# Can $\Delta^{14}CO_2$ observations help atmospheric inversions constrain the fossil $CO_2$ emission budget of Europe?

Carlos Gómez-Ortiz[1], Guillaume Monteil[1], Sourish Basu[2,3], and Marko Scholze[1]

[1]Department of Physical Geography and Ecosystem Science, Lund University, Lund, Sweden
[2]Global Modeling and Assimilation Office, NASA Goddard Space Flight Center, Greenbelt, MD, USA
[3]Earth System Science Interdisciplinary Center, University of Maryland, College Park, MD, USA

**Correspondence:** Carlos Gómez-Ortiz (carlos.gomez@nateko.lu.se)

**Abstract.** Independent estimation and verification of fossil $CO_2$ emissions on a regional and national scale ~~is crucial to evaluate~~ are crucial for evaluating the fossil $CO_2$ emissions and reductions reported by countries as part of their ~~nationally determined contributions~~ Nationally Determined Contributions (NDCs). Top-down methods, such as the assimilation of *in situ* and satellite observations of different tracers (e.g., $CO_2$, CO, ~~$\Delta^{14}CO_2$~~$\Delta^{14}CO_2$, $XCO_2$), have been increasingly used ~~lately~~ for this purpose. In this paper, we use the Lund University Modular Inversion Algorithm (LUMIA) to estimate fossil $CO_2$ emissions and natural fluxes by ~~inverting simultaneously~~ simultaneously inverting *in situ* observations of $CO_2$ and ~~$\Delta^{14}CO_2$~~ $\Delta^{14}CO_2$ over Europe. We evaluate the inversion system by ~~performing~~ conducting a series of Observing System Simulation Experiments (OSSEs). We find that in regions with a dense sampling network, such as Western/Central Europe, ~~when we add $\Delta^{14}CO_2$~~ adding $\Delta^{14}CO_2$ observations in an experiment where the prior fossil $CO_2$ and biosphere fluxes are set to zero ~~, LUMIA is capable of recovering~~ allows LUMIA to recover the time series of both categories~~, reducing the prior to truth~~. This reduces the prior-to-truth root mean square error (RMSE) from 1.26 TgC day$^{-1}$ to 0.12 TgC day$^{-1}$ in fossil $CO_2$ and from 0.97 TgC day$^{-1}$ to 0.17 TgC day$^{-1}$ in biosphere ~~, and~~ fluxes, reflecting the true total $CO_2$ budget ~~in~~ by 91%. In a second set of experiments ~~,~~ using realistic prior fluxes, we find that ~~,~~in addition to retrieving the time series of the optimized fluxes, we are able to recover the true regional fossil $CO_2$ budget in Western/Central Europe by 95% and in Germany by 97%. In regions with low sampling coverage, such as Southern Europe and the British Isles, the posterior fossil $CO_2$ emissions are not ~~well resolved~~ well-resolved in any scenario~~, and~~. Moreover, the biosphere fluxes can follow the seasonality with a significant bias~~that makes~~, making it impossible to close the total $CO_2$ budget. We find that the prior uncertainty of fossil $CO_2$ emissions does not significantly impact the posterior estimates, showing similar results in regions with good sampling coverage like Western/Central and Northern Europe. Finally, ~~it is important to have~~ having a good prior estimate of the terrestrial isotopic disequilibrium ~~to avoid including additional noise to~~ is important to avoid introducing additional noise into the posterior fossil $CO_2$ fluxes.

## 1 Introduction

Carbon dioxide ($CO_2$) ~~emissions~~ from fossil fuels and cement production ~~became~~ has become the dominant source of anthropogenic emissions to the atmosphere from around 1950, leading to a concentration of $CO_2$ in the atmosphere of 419.70 ppm on September 16~~th~~th, 2023, 49% above pre-industrial levels (https://gml.noaa.gov/ccgg/trends/gl_trend.html, accessed

September 18~~th~~th, 2023). Although land and ocean sinks of $CO_2$ have increased over the past six decades, the fraction of emissions removed from the atmosphere is expected to decline as the $CO_2$ concentration increases; therefore, a higher proportion of emitted $CO_2$ will remain in the atmosphere (Eyring et al., 2021). Monitoring ~~the~~ $CO_2$ emissions and removals is important to follow compliance with international treaties such as the Paris Agreement (UNFCCC, 2016). In the Agreement, the Parties have committed to report their emissions and removals of $CO_2$ and other greenhouse gases (GHGs) to the United Nations Framework Convention on Climate Change (UNFCCC) through the annual GHG ~~inventories~~inventory. In the case of fossil $CO_2$ emissions, these inventories have been reported to have uncertainties between 5% and 10% in developed countries~~, and commonly used spatialized emission inventories such as EDGAR (~~. These annual inventories and other national-level data are used to spatially and temporally distribute $CO_2$ emissions at sub-national and sub-annual scales. These spatially distributed products help us to better understand the sources of $CO_2$ emissions and to implement more effective policies toward emission reduction (Han et al., 2020). Commonly available emission products, such as the Carbon Dioxide Information and Analysis Center (CDIAC) FFCO$_2$ emission maps (Andres et al., 2011), the Open-source Data Inventory for Anthropogenic $CO_2$ (ODIAC) emission data product (Oda and Maksyutov, 2011; Oda et al., 2018), and the Emissions Database for Global Atmospheric Research ~~) report~~ (EDGAR) (Janssens-Maenhout et al., 2019), use national energy statistics, power plant emission data, and spatial proxies such as nighttime light observations, population data, and road transport networks to spatially and temporally distribute the emissions. This additional information introduces new uncertainties that, in EDGAR, for instance, can reach a global uncertainty of approximately 11% (Solazzo et al., 2021)~~. However, uncertainties in estimating fossil $CO_2$ emissions could~~ , or can be as high as 120% in the case of CDIAC (Andres et al., 2016). These uncertainties can be more significant and challenging to characterize at sub-annual and sub-national scales, even in developed countries ~~(Basu et al., 2016; Miller et al., 2012; Han et al., 2020)~~(Basu et al., 2016; Miller et al., 2012).

~~Constraining fossil $CO_2$ emissions to sub-annual and sub-national scales is important to improve the accuracy of the GHG inventories. One way of performing this constraint is using~~ These emission products can be used alongside atmospheric observations of $CO_2$ ~~to improve the knowledge on the~~ and other tracers in inverse modeling systems to reduce their uncertainty, enhance our understanding of fossil $CO_2$ ~~fluxes, known as well as inverse modeling~~emissions and natural fluxes, and improve the accuracy of national carbon budgets. So far, atmospheric $CO_2$ inversion frameworks have predominantly been used to constrain terrestrial sources and sinks of $CO_2$ (Basu et al., 2013; Chevallier et al., 2007; Monteil et al., 2020; Monteil and Scholze, 2021). To constrain the terrestrial carbon cycle, inverse modelers ~~usually~~ typically prescribe fossil $CO_2$ fluxes from emission ~~inventories, assuming~~ data products, like those mentioned previously, assuming them to be perfectly well-known~~,~~. This is to avoid any bias ~~in~~ the fossil $CO_2$ flux ~~influence~~ might introduce to the estimates of ~~the biosphere flux (Turnbull et al., 2009). $CO_2$ atmospheric concentrations~~ terrestrial fluxes (Turnbull et al., 2009). The atmospheric concentrations of $CO_2$ represent a mixture of all sources, ~~where the biosphere signal is~~ with the natural signal being predominant during most of the year (~~growing season covering~~ the growing season covers spring to fall), masking the contribution of fossil $CO_2$ emissions (Shiga et al., 2014). ~~This means that~~ Consequently, additional information is necessary to ~~separate the fossil apportionment~~ segregate the fossil contribution from the natural signal in ~~$CO_2$ atmospheric observations to be able to~~ atmospheric $CO_2$ observations to constrain the fossil $CO_2$ fluxes. Some ~~attempts~~ strategies have included sampling ~~strategies where the~~ approaches where observations are taken close to ~~the largest~~ major fossil $CO_2$ sources (e.g., cities and power plants) (Bréon et al., 2015), or satellite observations of large point sources such as column-integrated atmospheric $CO_2$ concentration ($XCO_2$) (Kaminski et al., 2022; Wang et al., 2020). A more commonly ~~used approach~~ employed method is to combine these $CO_2$-only observations (either $CO_2$ or $XCO_2$) with additional tracers such as $NO_2$ and the $NO_x$:$CO_2$ ratio (Kuhlmann et al., 2021), or ground observations of ~~CO~~ CO (Newman et al., 2013; Brioude et al., 2013), APO (Atmospheric Potential Oxygen) (Pickers et al., 2022), and~~more widely ,~~ , more widely, the radiocarbon (~~$\Delta^{14}CO_2$~~$\Delta^{14}CO_2$) content of carbon dioxide (Turnbull et al., 2009; Basu et al., 2016; Wang et al., 2018)~~that~~ , which we use in this study.

Radiocarbon is the radioactive isotope of carbon with a half-life ~~time of ∼~~of approximately 5730 years and is produced naturally in the upper atmosphere by cosmic-ray-induced reactions with nitrogen (Turnbull et al., 2009). Fossil $CO_2$ does not contain radiocarbon (it has already decayed), and adding its $^{14}C$-free emissions to the atmosphere causes a depletion of $\Delta^{14}CO_2$ (Suess, 1955). Meanwhile, radiocarbon is being absorbed and released by the ocean and the biosphere, making it ~~a good~~ an effective tracer of the natural carbon cycle and, therefore, a tool to distinguish fossil emissions from ~~this~~ the natural cycle signal in atmospheric $CO_2$ observations (Turnbull et al., 2009, 2022; Zazzeri et al., 2023). Radiocarbon is also produced as a by-product of nuclear facilities (e.g., nuclear power plants) and atmospheric nuclear weapon tests, the latter occurring mostly between 1945 and 1980~~(~~, with the highest intensity in 1961-1962 ~~)~~ (Naegler and Levin, 2006). These bomb tests caused a ~~large~~ significant disturbance in the radiocarbon ~~cycling~~cycle, resulting in ~~a~~ an isotopic disequilibrium in the biosphere and ocean ~~isotopic disequilibrium~~(Hesshaimer et al., 1994). Isotopic disequilibrium is the difference between the isotopic signatures or radiocarbon content of carbon entering and leaving a pool. Despite its similar meaning, this occurs differently in the ocean and the biosphere. In the ocean, the disequilibrium results from $\Delta^{14}C$-depleted $CO_2$ from water that has returned to the surface and was out of contact with the atmosphere, ~~so the radiocarbon has decayed~~ allowing the radiocarbon to decay significantly. In the biosphere, the disequilibrium ~~results from~~ is a result of the heterotrophic respiration of $\Delta^{14}C$-enriched $CO_2$ assimilated a couple of decades ago when the atmospheric $\Delta^{14}C$ was higher due to the bomb spike (Lehman et al., 2013). Therefore, the ocean disequilibrium flux tends to dilute the atmospheric $\Delta^{14}C$ content, whereas the biosphere disequilibrium flux tends to enrich it.

The usefulness of atmospheric $\Delta^{14}CO_2$ observations ~~to estimate~~ in estimating the fossil $CO_2$ content in the atmosphere as a fraction of the total atmospheric $CO_2$ concentration has ~~already~~ been demonstrated in various modeling studies~~(Levin and Karstens, 2007; T~~ ~~. Nevertheless~~. For instance, Levin and Karstens (2007) present an observational approach to estimate hourly regional fossil fuel $CO_2$ offsets at a continental site (Heidelberg, Germany), using weekly mean $^{14}CO_2$-based fossil fuel $CO_2$ mixing ratios and CO observations. On a larger scale, Levin et al. (2008) examine monthly mean $^{14}CO_2$ observations from two German stations (Schauinsland and Heidelberg), compared against background measurements from Jungfraujoch, to assess the regional fossil fuel $CO_2$ surplus and emphasize the importance of high-precision radiocarbon measurements for quantifying fossil fuel $CO_2$ contributions at a regional scale in Europe. The study by Miller et al. (2012) explores the relationship between fossil fuel $CO_2$ emissions and enhancements in atmospheric concentrations of $^{14}CO_2$ and other anthropogenic trace gases. Utilizing a six-year dataset from vertical profiles in the northeast U.S., they separate the fossil and natural components of atmospheric $CO_2$ using apparent emission ratios of various gases to fossil fuel $CO_2$, offering observationally-based estimates of national emissions and comparing these with inventory-based estimates. Turnbull et al. (2015) use measurements of $CO_2$, $^{14}CO_2$, and CO from multiple sampling towers around Indianapolis, U.S., to differentiate fossil fuel $CO_2$ from background levels in an urban environment and evaluate the consistency of a bottom-up emission product. More recently, by using radiocarbon observations in $CH_4$ ($\Delta^{14}CH_4$) and $CO_2$ ($\Delta^{14}CO_2$) over London, Zazzeri et al. (2023) reveal that fossil fractions of $CH_4$ and atmospheric concentrations of fossil $CO_2$ are consistently higher than those predicted by simulations using emission products such as EDGAR. This discrepancy highlights the potential of $^{14}CO_2$ measurements to refine our understanding of fossil and biospheric $CO_2$ and $CH_4$ partitioning in urban settings, especially when the influence of nuclear power plants is minimal.

Nevertheless, large-scale four-dimensional inversion systems have only recently ~~included~~ begun to include $\Delta^{14}CO_2$ as an additional tracer to constrain fossil $CO_2$ emissions~~(Basu et al., 2016, 2020; Wang et al., 2018). Results from Observing System Simulation Experiments (OSSE)based on synthetic observations , assuming the current as well as an anticipated future network of~~ . Basu et al. (2016) introduced a novel dual-tracer atmospheric inversion technique that differentiates between biospheric and fossil fuel $CO_2$ fluxes using atmospheric $CO_2$ and $\Delta^{14}CO_2$ ~~measurement stations, have shown the high potential of constraining fossil~~ measurements over the U.S. This method not only allows for the estimation of monthly regional fossil fuel $CO_2$ fluxes but also addresses biases in biospheric flux estimates that occur when using traditional $CO_2$-only inversion methods with fixed fossil fuel flux assumptions. Their approach represents a significant advancement in quantifying regional and national fossil fuel emissions from atmospheric observations. Building upon this study, Basu et al. (2020) presented a more focused analysis in providing national and sub-national-scale estimates of fossil fuel $CO_2$ emissions, using an extensive observation database of both $CO_2$ and $\Delta^{14}CO_2$. Graven et al. (2018) conducted an in-depth analysis of fossil fuel $CO_2$ emissions in California, utilizing atmospheric observations from nine sites and employing the Weather Research and Forecasting model along with the Stochastic Time-Inverted Lagrangian Transport model (WRF-STILT). The research integrates measurements of $CO_2$ concentration and $\Delta^{14}CO_2$, uniquely combining these observations with high-resolution emission data from Vulcan v2.2 and EDGARv4.2, aiming to refine estimates of regional fossil fuel $CO_2$ emissions and explore the impact of various factors such as nuclear industry emissions and air-sea exchanges on atmospheric $CO_2$ levels. In Europe, Wang et al. (2018) evaluated the potential of a $\Delta^{14}CO_2$ observation network for estimating regional fossil fuel $CO_2$ emissions ~~over North America (Basu et al., 2016, 2020) and Europe (Wang et al., 2018). Having~~ through atmospheric inversions. They examined the effectiveness of different network configurations, from minimal to very dense setups, in reducing uncertainties in fossil $CO_2$ emissions estimation. The study used synthetic observations and the LMDZv4 global transport model, paying special attention to representation and aggregation errors. Establishing a network of both $CO_2$ and $\Delta^{14}CO_2$ measurement stations requires significant investments to ~~guarantee~~ ensure long monitoring periods that allow the identification of ~~the~~ sub-annual and sub-national scale variations in fossil $CO_2$ emissions. ~~In Europe, the~~ The Integrated Carbon Observation System (ICOS) atmospheric network includes 39 stations in 14 European countries and overseas territories. Hourly $CO_2$ atmospheric observations are available for 26 stations, with the earliest data from 2015 when the network was ~~created~~established. However, some of these stations already existed by then, and there is information from previous years. Fourteen stations measure $\Delta^{14}CO_2$ in ~~2-weekly~~ 2-week integrated samples analyzed by the ICOS Central Radiocarbon Laboratory. The ICOS network is expanding to include more stations, and new sampling strategies are being developed to increase the number of $\Delta^{14}CO_2$ measurements.

In this work, we explore the interest of using ~~these~~ $CO_2$ and $\Delta^{14}CO_2$ observations to constrain the fossil $CO_2$ emissions in Europe. For this purpose, we expanded the ~~LUMIA~~ Lund University Modular Inversion Algorithm (LUMIA) system (Monteil and Scholze, 2021) to perform simultaneous inversions of atmospheric $CO_2$ and $\Delta^{14}CO_2$, thus optimizing ~~the~~ fossil emissions, natural fluxes, and ~~the~~ isotopic disequilibrium. We perform ~~observing system simulation experiments~~ Observing System Simulation Experiments (OSSEs), recreating the current state of the ICOS network and its sampling strategy, and using different flux products (as priors and true values) to demonstrate the performance of the inversion scheme and show its capabilities. We begin by assessing the impact of oceanic fluxes on the total $CO_2$ and $\Delta^{14}CO_2$ concentrations. Then, we evaluate the impact of adding $\Delta^{14}CO_2$ observations on the estimation of fossil $CO_2$ emissions by comparing the model's ability to recover true fluxes starting from a prior flux set to zero. Finally, with a more realistic setup, i.e., prior, we evaluate the impact of the prescribed fossil $CO_2$ flux uncertainty and the impact of the terrestrial isotopic disequilibrium product.

## 2 Theoretical background

The depletion of radiocarbon in the atmosphere due to fossil $CO_2$ emissions has been demonstrated in various studies since the 1950s, ~~mainly from~~ primarily through the $\Delta^{14}C$ content in tree rings (Suess, 1955; Tans et al., 1979). Anthropogenic disturbances in ~~the~~ atmospheric radiocarbon content, such as ~~the~~ those from nuclear bomb tests and ~~the~~ nuclear power facilities (Hesshaimer and Levin, 2000), ~~led to the study and better~~ have led to a deeper understanding of the radiocarbon exchange processes between the atmosphere~~and~~ , the biosphere (Hahn et al., 2006), and the ocean (Hesshaimer et al., 1994).

With ~~later improvements in the~~ subsequent advancements in measurement and modeling techniques, $\Delta^{14}CO_2$ observations ~~were~~ have been used to estimate the fossil $CO_2$ offset ~~in~~ within atmospheric $CO_2$ ~~(Levin and Hesshaimer, 2000; Kuc et al., 2003; Naegler an~~ concentrations (Levin and Hesshaimer, 2000; Kuc et al., 2003; Naegler and Levin, 2006; Levin and Karstens, 2007; Levin et al., 2008) . This is achieved by comparing observations from free troposphere background stations against ~~regional~~ those from regionally polluted stations, ~~becoming an important precursor~~ establishing an essential foundation for estimating fossil $CO_2$ emissions using inverse modeling~~as we describe~~ , as will be discussed in the following sections.

### 2.1 Regional transport model

We perform the inversions for a regional domain ranging from 15°W, 33°N to 35°E, 73°N (depicted in Figure 1, corresponding to the one used in previous studies, e.g., Monteil et al. (2020) and Thompson et al. (2020)).

The link between the surface C fluxes and the $CO_2$ and $\Delta^{14}CO_2$ concentrations, following the implementation of Rödenbeck et al. (2009), is defined as::

$$y^i_{\mathrm{CO_2}} = y^i_{\mathrm{bg[CO_2]}} + \sum_c H(F_\mathrm{c}) \tag{1a}$$

$$y^i_{\mathrm{C\Delta^{14}C}} = y^i_{\mathrm{bg[C\Delta^{14}C]}} + \sum_c H(\Delta_\mathrm{c} F_\mathrm{c}) \tag{1b}$$

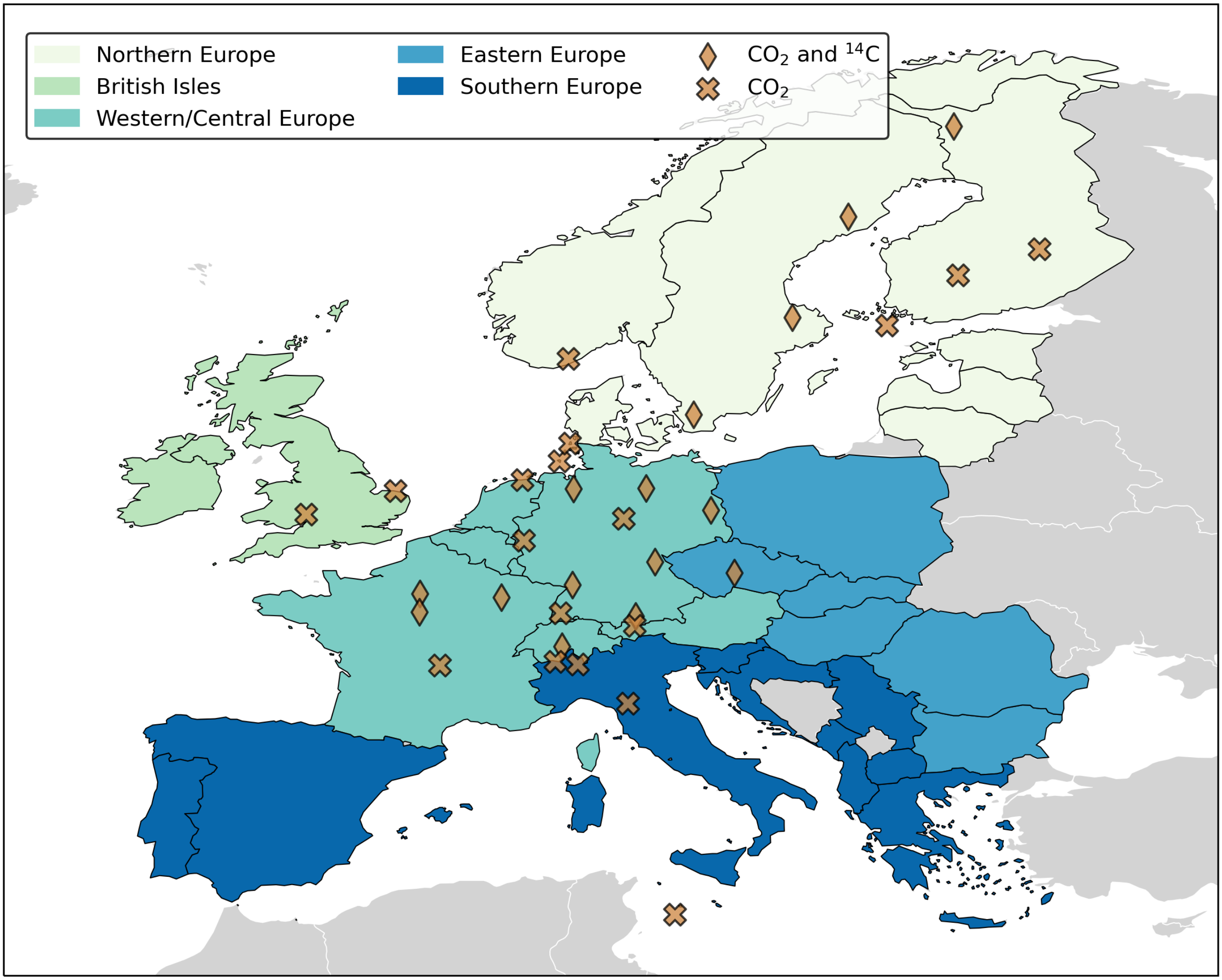

**Figure 1.** Study domain and location of the ICOS Atmosphere network sampling stations used in this paper. The regions will be used for the analysis and discussion of the results.

where $y^i$ is the modeled concentration corresponding to ~~the~~ observation $i$, $y^i_{\mathrm{bg}}$ is the modeled background concentration (i.e., boundary condition) (see Section 3.3). The operator $H$ represents the regional transport model (see Section 3.2), which is used to calculate the contribution of surface fluxes $F$ (in each category $c$) to the change of $\mathrm{CO_2}$ and $\Delta^{14}\mathrm{CO_2}$ in the atmosphere. $F_c$ in this study corresponds to gridded fluxes in a resolution of 0.5° × 0.5° and 1-hourly. In Eq. 1b, the term $\Delta_c$ refers to the $\Delta^{14}\mathrm{CO_2}$ signature of the accompanying flux category (Tans et al., 1979; Turnbull et al., 2016). Since $\Delta^{14}\mathrm{CO_2}$ ‰ ~~-~~values are not additive, and following Basu et al. (2016), we convert all values to $\mathrm{CO_2}\Delta^{14}\mathrm{CO_2}$ values (or $\mathrm{C}\Delta^{14}\mathrm{C}$ for simplification)~~. This means that~~, meaning we do not model $\Delta^{14}\mathrm{CO_2}$ in ‰ (permil) units, as reported in observations ($\Delta^{14}\mathrm{CO_2}$), but in units of amount of $CO_2$ × ‰ (e.g., $CO_2$ ~~ppm‰~~ ppm for concentrations, PgC‰ $yr^{-1}$ for fluxes). The capital delta notation ($\Delta^{14}CO_2$ or just Δ), usually expressed in units of permil (‰ ~~is the enrichment of~~ ), represents the enrichment or depletion of the atmosphere relative to a standard (Stuiver and Polach, 1977), ~~that~~ in this case, ~~is~~ the amount of radiocarbon relative to an absolute standard of $^{14}C$ from 1950 (Trumbore et al., 2016), meaning that positive values indicate ~~that~~ the $^{14}C$ content in the sample is higher than the pre-industrial atmosphere.

Expanding the foreground part of Equation 1 to include the flux categories ~~yields explicitly~~ explicitly yields:

$$\sum_{c} H(F_{\mathrm{c}}) = H(F_{\mathrm{ff}}) + H(F_{\mathrm{bio}}) + H(F_{\mathrm{oce}}) \tag{2a}$$

where $F_{\mathrm{ff}}$ is the fossil $CO_2$ emissions, $F_{\mathrm{bio}}$ is the net $CO_2$ flux between the atmosphere and ~~the~~ terrestrial ecosystems (Net Ecosystem Exchange, NEE, ~~in the following~~ hereafter also called biosphere flux), and $F_{\mathrm{oce}}$ is the atmosphere-ocean $CO_2$ exchanges. ~~The reason to calculate~~ Calculating each $H(F_{\mathrm{c}})$ ~~is to keep track of~~ separately tracks the influence of each category~~and~~ , not just the total. For radiocarbon, the equation looks similar but includes an additional term for the radiocarbon from nuclear facilities:

$$\begin{aligned}\sum_{c} H(\Delta_{\mathrm{c}} F_{\mathrm{c}}) =& H(\Delta_{\mathrm{ff}} F_{\mathrm{ff}}) + H(\Delta_{\mathrm{atm}}(F_{\mathrm{bio}} + F_{\mathrm{oce}})) + H(F_{\mathrm{bio2atm}}(\Delta_{\mathrm{bio}} - \Delta_{\mathrm{atm}})) \qquad (2b)\\ &+ H(F_{\mathrm{oce2atm}}(\Delta_{\mathrm{oce}} - \Delta_{\mathrm{atm}})) + H(\Delta_{\mathrm{nuc}} F_{\mathrm{nuc}})\\ =& H(\Delta_{\mathrm{ff}} F_{\mathrm{ff}}) + H(\Delta_{atm}(F_{\mathrm{bio}} + F_{\mathrm{oce}})) + H(F_{\mathrm{biodis}}) + H(F_{\mathrm{ocedis}}) + H(\Delta_{\mathrm{nuc}} F_{\mathrm{nuc}}) \qquad (2c)\end{aligned}$$

where $\Delta_{\mathrm{ff}}$ is set equal to -1000‰, indicating that fossil $CO_2$ does not contain any $\Delta^{14}CO_2$ and, therefore, ~~the fossil $CO_2$ emissions will dilute the~~ dilutes the atmospheric $\Delta^{14}CO_2$ content. $\Delta_{\mathrm{atm}} F_{\mathrm{bio}}$ and $\Delta_{\mathrm{atm}} F_{\mathrm{oce}}$ refer to the exchange of "modern" $C\Delta^{14}C$ between ~~the~~ terrestrial ecosystems and the ocean, respectively, with the atmosphere, since $\Delta^{14}C$ in new biomass and the top ocean ~~would be nearly the same as~~ layer would nearly match atmospheric $\Delta^{14}C$ ($\Delta_{\mathrm{atm}}$) (Graven et al., 2020). $F_{\mathrm{biodis}}$ and $F_{\mathrm{ocedis}}$ ~~correspond to~~ represent the isotopic disequilibrium, or the isotopic difference between the source (ocean or biosphere) and the atmosphere. $F_{\mathrm{biodis}}$ is ~~the~~ "old-captured" and $\Delta^{14}C$-enriched $C\Delta^{14}C$ released through heterotrophic respiration ($F_{\mathrm{bio2atm}}$). $F_{\mathrm{ocedis}}$ is ~~the~~ "old-captured" and $\Delta^{14}C$-depleted $C\Delta^{14}C$ released through vertical transport of water masses ($F_{\mathrm{oce2atm}}$) (Lehman et al., 2013; Basu et al., 2016). $F_{\mathrm{nuc}}$ is the radiocarbon production due to ~~the~~ nuclear activities, mainly from nuclear facilities, since radiocarbon production from nuclear bomb tests has ~~been depleted nowadays~~ largely ceased (Hesshaimer and Levin, 2000). Converting $\Delta_{\mathrm{nuc}} F_{\mathrm{nuc}}$ to $C\Delta^{14}C$ notation, ~~to put it in modeling units~~ for modeling purposes as mentioned above, ~~yields~~is achieved through:

$$\Delta_{\mathrm{nuc}} F_{\mathrm{nuc}} = \frac{N}{r_{\mathrm{std}}} F_{\mathrm{nuc}} \tag{3}$$

where $r_{\mathrm{std}}$ is the ~~$^{14}C:C$ standard~~ standard $^{14}C:C$ ratio ($1.176 \times 10^{-12}$)~~and $N = (975/(\delta^{13}C + 1000))^2$~~ , and $N = (975/(\delta^{13}C + 1000))$ is the isotope fractionation correction ~~(Basu et al., 2016; Stuiver and Polach, 1977). Combining equations~~ (Stuiver and Polach, 1977)

. As the $\delta^{13}$C value, we use the global atmospheric yearly average of $-8‰$ (Basu et al., 2016). Combining Equations 1 through 3 ~~yields~~ for the modeled $CO_2$ and $\Delta^{14}CO_2$ concentrations yields:

$$y^i_{\mathrm{CO_2}} = y^i_{\mathrm{bg[CO_2]}} + H(F_{\mathrm{ff}}) + H(F_{\mathrm{bio}}) + H(F_{\mathrm{oce}}) \tag{4a}$$

$$y^i_{\mathrm{C\Delta^{14}C}} = y^i_{\mathrm{bg[C\Delta^{14}C]}} + H(\Delta_{\mathrm{ff}} F_{\mathrm{ff}}) + H(F_{\mathrm{biodis}}) + H(F_{\mathrm{ocedis}}) + H(\Delta_{atm}(F_{\mathrm{bio}} + F_{\mathrm{oce}})) + H(\frac{N}{r_{\mathrm{std}}} F_{\mathrm{nuc}}) \tag{4b}$$

~~There is an~~ An additional source of radiocarbon~~that is not included in Equation 4:~~ , the cosmogenic production~~. This cosmogenic radiocarbon production~~ , occurs naturally in the upper atmosphere due to cosmic-ray-induced reactions with nitrogen. This term is implicitly included in the background $y^i_{\mathrm{bg[C\Delta^{14}C]}}$.

## 2.2 Observations

The sampling stations ~~shown~~ depicted in Figure 1 ~~depict~~ represent the ICOS Atmosphere network for the years 2018-2020~~(~~, noting that new sampling stations have been added since ~~then)~~that period. The ICOS Atmosphere network is ~~part~~ a component of ICOS, a European research infrastructure ~~that aims~~ designed to provide long-term, high-quality, and harmonized ~~carbon observations . The Atmosphere network comprises~~ observations of carbon dynamics. The network includes 33 stations ~~distributed~~ across Europe, all measuring $CO_2$, ~~and~~ with 15 ~~stations additionally~~ of these stations also measuring $\Delta^{14}CO_2$. ~~Two sampling strategies are implemented~~

There are two sampling strategies employed at the ICOS stations: continuous and periodical sampling. Continuous sampling is ~~made in almost every sampling height available in~~ performed at nearly every available sampling height at the station, ~~using~~ utilizing commercially available automatic samplers ~~to take~~ for hourly measurements of~~e.g.~~ , for example, $CO_2$. Periodical sampling~~is made using flask samplers~~ , on the other hand, is conducted only at the highest sampling height ~~. The flasks are subsequently analyzed at the different~~ using flask samplers. These flasks are later analyzed in various ICOS laboratories. ~~There are 1-hour~~ Hourly integrated flask samples~~taken~~ , collected every three days~~that are used for quality control of~~ , serve both as quality control for the continuous sampling ~~, but as well~~ and for measuring other gases ~~that are not measured continuously (e.g.~~ not continuously monitored (e.g., $SF_6$, $H_2$, stable isotopes of $CO_2$), ~~and $\Delta^{14}$C for determining the~~ in addition to $\Delta^{14}CO_2$ for the determination of the atmospheric fossil $CO_2$ component through inverse modeling (Levin et al., 2020). ~~An additional~~ Furthermore, a 2-week integrated flask sample ~~passes the~~ is designed to pass air over a ~~solution of NaOH dedicated to $\Delta^{14}$C sampling.~~ NaOH solution, specifically for $\Delta^{14}CO_2$ sampling.

In this paper, we use the 1-hour $CO_2$ continuous and the 2-week integrated ~~$\Delta^{14}$C~~ $\Delta^{14}CO_2$ periodical sampling strategies for ~~evaluating~~ the evaluation of LUMIA. A summary of the stations, including their location, sampling height, number and average of measurements, and integration days~~is shown~~ , is presented in Table 1.

**Table 1.** Observation stations used in ~~the~~ this study. ~~As an example, we include~~ Included is a summary of the number of observations (N~~$_{obs}$~~$_{\mathrm{obs}}$), average observations ± one standard deviation, and the integration time of ~~$\Delta^{14}CO_2$~~ $\Delta^{14}$CO2 samples for the year 2018, ~~according to the~~ based on data ~~available~~ accessible through the ICOS Python API (https://pypi.org/project/icoscp/, accessed February 2023). Stations with zero ~~$N_{obs}$~~ $N_{\mathrm{obs}}$ did not measure or report observations of the corresponding tracer in 2018 to ICOS, but ~~we include them in~~ they are incorporated into this study for comprehensive analysis.

| **Code** | **Name** | **Country** | **Lat (°E)** | **Lon (°N)** | **Altitude (m.a.s.l)** | **Max. samp. height (m.a.g.l)** | **$N_{obs}$ $CO_2$** | **$N_{obs}$ $\Delta^{14}C$** | **Avg. $CO_2$ (ppm)** | **Avg. $\Delta^{14}C$ (‰)** | **Integration time (days)** |
|---|---|---|---|---|---|---|---|---|---|---|---|
| BIR | Birkenes | NO | 58.39 | 8.25 | 219 | 75 | 2616 | – | 421.9 ± 8.0 | – | – |
| CMN | Monte Cimone | IT | 44.19 | 10.70 | 2165 | 8 | 5832 | – | 406.3 ± 6.0 | – | – |
| GAT | Gartow | DE | 53.07 | 11.44 | 70 | 341 | 8784 | 0 | 419.5 ± 10.0 | – | – |
| HEL | Helgoland | DE | 54.18 | 7.88 | 43 | 110 | 1080 | – | 430.4 ± 10.1 | – | – |
| HPB | Hohenpeissenberg | DE | 47.8 | 11.02 | 934 | 131 | 8784 | 17 | 415.6 ± 6.8 | -4.1 ± 2.8 | 13.4 ± 0.5 |
| HTM | Hyltemossa | SE | 56.1 | 13.42 | 115 | 150 | 8784 | 21 | 417.1 ± 8.4 | -3.2 ± 3.2 | 14.0 ± 1.6 |
| IPR | Ispra | IT | 45.81 | 8.64 | 210 | 100 | 8784 | – | 430.0 ± 15.9 | – | – |
| JFJ | Jungfraujoch | CH | 46.55 | 7.99 | 3580 | 5 | 8784 | 15 | 413.1 ± 3.6 | -1.0 ± 3.5 | 14.0 ± 0.0 |
| JUE | Jülich | DE | 50.91 | 6.41 | 98 | 120 | 8784 | – | 423.0 ± 11.2 | – | – |
| KIT | Karlsruhe | DE | 49.09 | 8.42 | 110 | 200 | 8784 | 21 | 428.7 ± 17.5 | -14.1 ± 10.4 | 6.2 ± 0.7 |
| KRE | Křešín u Pacova | CZ | 49.57 | 15.08 | 534 | 250 | 8784 | 13 | 422.0 ± 11.5 | -4.1 ± 3.0 | 13.2 ± 0.6 |
| LIN | Lindenberg | DE | 52.17 | 14.12 | 73 | 98 | 8784 | 5 | 426.0 ± 13.1 | -8.6 ± 6.3 | 14.0 ± 0.0 |
| LMP | Lampedusa | IT | 35.52 | 12.63 | 45 | 8 | 8088 | – | 414.7 ± 4.2 | – | – |
| LUT | Lutjewad | NL | 53.4 | 6.35 | 1 | 60 | 8784 | – | 422.3 ± 12.2 | – | – |
| NOR | Norunda | SE | 60.09 | 17.48 | 46 | 100 | 8784 | 19 | 417.8 ± 8.2 | -0.7 ± 4.2 | 13.3 ± 0.5 |
| OPE | Observatoire pérenne de l'environnement | FR | 48.56 | 5.5 | 390 | 120 | 8784 | 17 | 420.2 ± 9.5 | -3.3 ± 3.5 | 13.5 ± 0.5 |
| OXK | Ochsenkopf | DE | 50.03 | 11.81 | 1022 | 163 | 8784 | 0 | 416.8 ± 6.4 | – | – |
| PAL | Pallas | FI | 67.97 | 24.12 | 565 | 12 | 8784 | 17 | 416.2 ± 7.7 | -1.5 ± 3.5 | 12.9 ± 1.9 |
| PRS | Plateau Rosa | IT | 45.93 | 7.70 | 3480 | 10 | 0 | – | – | – | – |
| PUI | Puijo | FI | 62.91 | 27.65 | 232 | 84 | 1248 | – | 426.6 ± 4.5 | – | – |
| PUY | Puy de Dôme | FR | 45.77 | 2.97 | 1465 | 10 | 8784 | – | 414.0 ± 5.4 | – | – |
| RGL | Ridge Hill | GB | 52.0 | -2.54 | 199 | 90 | 8784 | – | 413.4 ± 6.1 | – | – |
| SAC | Saclay | FR | 48.72 | 2.14 | 160 | 100 | 8784 | 12 | 420.5 ± 10.5 | -2.7 ± 6.4 | 16.5 ± 4.3 |
| SMR | Hyytiälä | FI | 61.85 | 24.29 | 181 | 125 | 8784 | – | 416.8 ± 8.5 | – | – |
| SSL | Schauinsland | DE | 47.92 | 7.92 | 1205 | 35 | 0 | – | – | – | – |
| STE | Steinkimmen | DE | 53.04 | 8.46 | 29 | 252 | 8784 | 13 | 421.9 ± 11.5 | -6.7 ± 4.2 | 13.5 ± 1.6 |
| SVB | Svartberget | SE | 64.26 | 19.77 | 269 | 150 | 8784 | 13 | 416.1 ± 8.0 | -0.9 ± 3.1 | 15.6 ± 1.9 |
| TOH | Torfhaus | DE | 51.81 | 10.54 | 801 | 147 | 8784 | – | 417.6 ± 7.8 | – | – |
| TRN | Trainou | FR | 47.96 | 2.11 | 131 | 180 | 8784 | 11 | 419.4 ± 8.6 | -4.7 ± 4.8 | 14.7 ± 3.3 |
| UTO | Utö - Baltic sea | FI | 59.78 | 21.37 | 8 | 57 | 8784 | – | 416.2 ± 8.0 | – | – |
| WAO | Weybourne | GB | 52.95 | 1.12 | 31 | 10 | 8784 | – | 413.4 ± 6.1 | – | – |
| WES | Westerland | DE | 54.92 | 8.31 | 12 | 14 | 8784 | – | 416.2 ± 2.7 | – | – |
| ZSF | Zugspitze | DE | 47.42 | 10.98 | 2666 | 3 | 0 | – | – | – | – |

### 2.3 Inverse modeling problem

Atmospheric inverse modeling can be used for a variety of purposes, including the establishment of the initial conditions of a model, the identification of sources and sinks, and the evaluation and improvement of ~~emission inventories~~ prior emissions (Bocquet et al., 2015). The goal is to estimate the best set of variables (fluxes) consistent with atmospheric measurements of a tracer (e.g. $CO_2$ and $\Delta^{14}CO_2$) in the study domain (observations), given the atmospheric transport that relates the two. In its most basic form, this can be formulated as

$$y = H(x,b) + \epsilon \tag{5}$$

where the control vector $x$ contains the variables (carbon fluxes, $F_c$) to be estimated, and the observation vector $y$ contains the observations (atmospheric concentrations). $H$ is the observation operator, which includes the transport model and any additional observations processing, such as accounting for the boundary conditions and variables, $b$, that we will not optimize. $\epsilon$ is the error vector that includes the errors in the observations, the transport model, and the control vector.

There are multiple approaches to solving the inverse modeling problem. In this paper, and in general in LUMIA, we use the variational approach, in which the control vector $x$ that minimizes the cost function in Eq. 6 is sought iteratively by minimizing the misfit between the model outputs and the observations that are available over a range of times, also known assimilation window (Chatterjee and Michalak, 2013; Rayner et al., 2019; Scholze et al., 2017):

$$J(x) = \frac{1}{2}(x - x_b)^T \underline{B}\mathbf{B}^{-1}(x - x_b) + \frac{1}{2}\left(\underline{Hx - y}\mathbf{H}x - y\right)^T \underline{R}\mathbf{R}^{-1}\left(\underline{Hx - y}\mathbf{H}x - y\right) \tag{6}$$

where ~~$B$~~ $\mathbf{B}$ is the prior uncertainty covariance matrix, and ~~$R$~~ $\mathbf{R}$ is the observational uncertainty covariance matrix, controlling the weight of each observation and target variable in the optimization. The iterative procedure searches for the value of $x$ that ~~minimizes~~ minimize $J(x)$, i.e. the value of $x$ for which the gradient $(\nabla_x J)$ is equal to zero. The observation operator $H(x)$ can be expressed as the Jacobian matrix ~~$Hx$~~ $\mathbf{H}x$ that stores the sensitivity of each observation to each control vector element (Monteil and Scholze, 2021).

#### 2.3.1 Construction of the control vector ($x$)

The control vector $x$ contains the set of parameters adjustable by the inversion, which are offsets to the different sources and sinks of $CO_2$ and $\Delta^{14}CO_2$ that we want to estimate. From Equation 4, our main interest is to optimize the fossil $CO_2$ flux $F_{\mathrm{ff}}$. But, since through the radiocarbon cycle, we can separate the fossil and the natural $CO_2$, we also need to optimize the fluxes from the biosphere ($F_{\mathrm{bio}}$), as well as the isotopic disequilibrium $F_{\mathrm{biodis}}$, to reduce the uncertainty from these two terms that can have an important impact on the inversion result. The remaining fluxes ($F_{\mathrm{nuc}}$, $F_{\mathrm{oce}}$, and $F_{\mathrm{ocedis}}$) are prescribed and not included in the control vector.

~~In order to~~ To limit the computational requirements, we do not solve directly for the high-resolution fluxes (e.g. 0.5° × 0.5° and 1-hourly) used in the transport model, but for weekly offsets for 2500 clusters of grid points. Appendix B describes

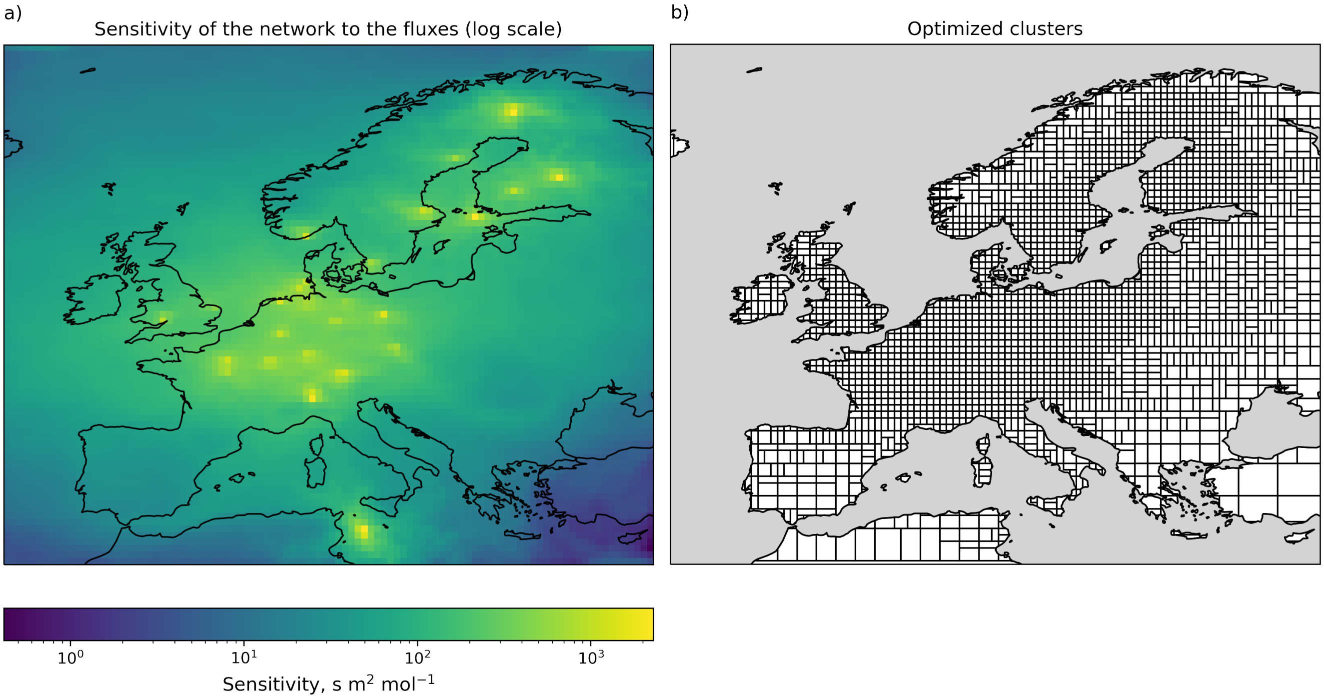

**Figure 2.** Visual representation of a) the sensitivity of the observation network to each grid-cell (in logarithmic scale) and b) the optimized clusters and their variable spatial resolution.

the clustering algorithm in further detail. In short, it groups ~~together~~ contiguous grid cells, depending on how sensitive the observation network is to their emissions: grid cells directly upwind of the sampling stations are optimized at the native resolution of 0.5°, but in parts of the domain not well sampled by the observations (e.g. North Africa, Turkey), the resolution drops down to 5° × 3.5° (see Figure 2).

The relation between the control vector and the gridded emissions is given by:

$$\underline{F}\mathbf{F}_c = \underline{F}\mathbf{F}_c^0 + \mathbf{T}_T \mathbf{X}_x^c \mathbf{T}_H \qquad (7)$$

where ~~$F_c$ is the vector~~ $\mathbf{F}_c$ is the matrix containing gridded emissions for the category $c$, with prior value ~~$F_c^0$~~$\mathbf{F}_c^0$. The matrix $\mathbf{X}_x^c$ is the portion of the control vector $x$ that contains offsets for the category $c$, reshaped as a $(n_{opt}^t, n_{opt}^p)$ matrix, with $n_{opt}^t$ and $n_{opt}^p$ the number of optimized (weekly) ~~time steps~~ intervals and grid-cell clusters, respectively. The matrices $\mathbf{T}_t$ $(n_{mod}^t, n_{opt}^t)$ and $\mathbf{T}_H$ $(n_{opt}^p, n_{mod}^p)$ contain the relative contribution of each model time step $t_{mod}$ (1 hour) and of each grid-cell $p_{mod}$ (0.5° × 0.5°) to each optimized time-step $t_{opt}$ and cluster $p_{mod}$. To reduce the number of iterations and large matrix multiplications, the optimization is performed on a preconditioned control vector $\omega = \mathbf{B}^{-1/2}(x - x_b)$. More information about the preconditioning can be found in Monteil and Scholze (2021).

### 2.3.2 Construction of the prior error covariance matrix ($\mathbf{B}$)

Our matrix $\mathbf{B}$ is constructed such that we first determine the spatio-temporal structure of the uncertainties, which is then scaled to match the reported uncertainties. Since we are optimizing for offsets, the prior control vector $x_b$ contains only zeros (so $F_c = F_c^0$). The uncertainties on $x_b$ are given by the error covariance matrix $\mathbf{B}$. We assume no correlation between different categories and different tracers. Therefore, the sections of $\mathbf{B}$ specific to each tracer/category can be constructed independently. We do this in three steps:

1. Construct a vector of variances (diagonals of $\mathbf{B}$), which contain the spatio-temporal pattern of the uncertainties.

2. Construct the covariances based on spatial and temporal correlation functions. Specifically, the covariances are set following $cov(x_1, x_2) = \sigma_{x_1}\sigma_{x_2}e^{-(d(p1,p2)/L_h)^2}e^{-|t2-t1|/L_t}$, with $d(p1, p2)$ the geographical distance between the center of the clusters (area-weighted average of the center-coordinates of the grid-cells in the cluster), and $|t2-t1|$ the temporal distance between $x_1$ and $x_2$.

3. Scale the entire (section of the) $\mathbf{B}$ matrix by a uniform scaling factor to match a prescribed category-specific annual uncertainty value $\delta F_c$.

The values of correlation lengths $L_h$ and $L_t$, as well as the scaling factors $\delta F_c$ are provided in Section 3.3.1. For constructing the vector of variances ($\sigma_x^2$), two approaches were used:

- For fossil $CO_2$ emissions $F_{\text{ff}}$, the variance is set to $\sigma^2_{p,t,c} = |\sum_{i,j,t_{mod}} F^c_{i,j,t_{mod}}|^2$, where $\sigma^2_{p,t,c}$ is the variance corresponding to the control vector elements for the ~~time step ~~interval $t$ and spatial cluster $p$ of category $c$. The spatial coordinates $i$ and $j$ are the ensemble of grid cells that are within the cluster $p$, and the temporal coordinate $t_{mod}$ is the ensemble of 1-hourly model time steps that are within the (weekly) optimization ~~time-step ~~interval $t$. For instance, if the cluster $p$ groups four model ~~grid-cells~~grid cells, the variance $\sigma^2_{p,t,c}$ will be calculated over 672 flux components (4 ~~grid-cells~~grid cells, seven days with 24 hourly time steps).

- For the other fluxes, the procedure is similar, but the formula is $\sigma^2_{p,t,c} = \sqrt{|\sum_{i,j,t_{mod}} F^c_{i,j,t_{mod}}|}$.

The rationale behind these formulas is to scale the uncertainties to the prior estimate of the fluxes (assuming that very low prior fluxes should imply low prior uncertainties) but avoid artificially low errors in instances where negative and positive fluxes compensate each other (i.e., NEE, in the spring and autumn times). Furthermore, the location of fossil $CO_2$ emissions is relatively better known. Therefore, the formula used for fossil $CO_2$ emissions concentrates the uncertainties more at the location of prior emissions than that used for the other categories. Regardless of the formula used for determining the variance, it is scaled afterward to match the target uncertainty reported in Table 2.

## 3 Observing System Simulation Experiments (OSSEs)

~~In order to~~ To assess the performance of the inversion system, we designed and performed a series of Observing System Simulation Experiments (OSSEs). In so-called OSSEs, the impact of new observing systems, configurations of existing systems, observing strategies, and the optimization of new data are evaluated (Hoffman and Atlas, 2016). This is done by generating a set of simulated observations, called synthetic observations, from a set of reasonable but arbitrary fluxes, $\hat{F}_c$, considered 'true' fluxes in the OSSE. Then, by using fluxes from different models or products as prior fluxes ($F_c$), we investigate the ability of an inverse modeling system to reconstruct the true fluxes consistent with the model setup (e.g. prescribed uncertainties, error structure), making assumptions such as a perfect transport and a perfect boundary condition. In the following sections, we describe the different data sets, model setups, assumptions, and experiments used in this study.

### 3.1 True and prior fluxes

We use a set of fluxes commonly used in this kind of inverse problem with a high horizontal and temporal resolution (0.5° × 0.5° and 1 hour, respectively) to generate our synthetic observations. For the $CO_2$ fluxes, we use EDGARv4.3 emission ~~inventory~~ database (Janssens-Maenhout et al., 2019) distributed spatially and temporally based on fuel type, category, and country-specific emissions, using the COFFEE approach (Steinbach et al., 2011) (EDGAR in Table 3, see (Gerbig and Koch, 2021b)) as $\hat{F}_{\text{ff}}$ for the base year 2018. For $\hat{F}_{\text{bio}}$, we use a simulation of the LPJ-GUESS vegetation model (Smith et al., 2014) (LPJ-GUESS in Table 3, see (Wu, 2023)), and for $\hat{F}_{\text{oce}}$, we use the Jena Carbo-Scope v1.5 product (Rödenbeck et al., 2013). We use the terrestrial and ocean disequilibrium and nuclear fluxes from Basu et al. (2020) as our $\hat{F}_{\text{biodis}}$ (BASU in Table 3), $\hat{F}_{\text{ocedis}}$ and $\hat{F}_{\text{nuc}}$, respectively.

As prior fluxes, we use products that followed different methodologies and schemes, with different spatial and temporal structures than the true fluxes, to make the implementation more realistic. For $F_{\text{ff}}$, we use a version of ODIAC (Open-source Data Inventory for Anthropogenic $CO_2$) (ODIAC in Table 3, see (Oda and Maksyutov, 2020)) with a 1km × 1km spatial and monthly temporal resolution. Thus, our prior fossil $CO_2$ fluxes include monthly variability but do not resolve the daily cycle (Oda et al., 2018). We also prepare a flat-year average version of this product (FlatODIAC in Table 3). For $F_{\text{bio}}$, we use a product from simulations of the VPRM vegetation model (Mahadevan et al., 2008; Thompson et al., 2020) (VPRM in Table 3, see (Gerbig and Koch, 2021a)). Due to the lack of an alternative product for the $F_{\text{biodis}}$, we generate our own prior by calculating a series of randomly perturbed versions of the true flux following their prescribed uncertainties and their horizontal and temporal correlations (RndBASU in Table 3). This perturbation is done by adding a random perturbation to the control vector and transforming such vector to the flux space. All fluxes are gridded to 0.5° × 0.5° and 1-hour resolution by the nearest neighbor interpolation.

### 3.2 Observation footprints (FLEXPART)

Similar to Monteil and Scholze (2021), we compute the regional transport (e.g. operator $H$ in Equation 4) using the FLEXPART 10.4 Lagrangian transport model (Pisso et al., 2019). For each observation, FLEXPART computes a "footprint", i.e. a vector containing the sensitivity of the observation to changes in the surface fluxes. The footprints are pre-computed and then used throughout the subsequent steps of the inversion (see Monteil and Scholze (2021) for further details). The FLEXPART

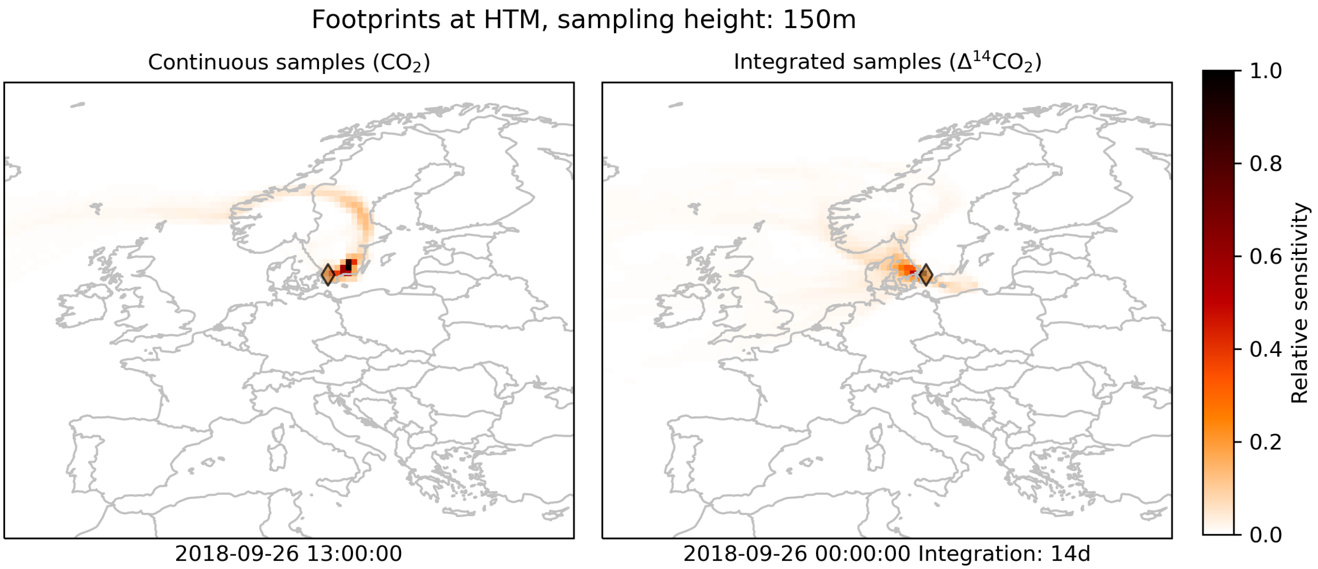

**Figure 3.** ~~Example~~ Examples of so-called (pre-calculated~~observations~~) footprints for $CO_2$ (left) and $\Delta^{14}CO_2$ (right) at the Hyltemossa ICOS station. ~~$\Delta^{14}CO_2$ (~~The maps show the sensitivity of the respective atmospheric tracer at the sampling site to the surface fluxes over the regional domain up to two weeks before the observation. The left panel displays the sensitivity of $CO_2$ at the indicated sampling time and shows influences by surface fluxes from the North Atlantic through Scandinavia, while the right ~~) has an~~ panel demonstrates the dispersed sensitivity of a 14-day integrated $\Delta^{14}CO_2$ sample across Northwestern Europe and the Baltic region. The two maps illustrate the distinct spatial integration ~~time~~ of ~~14 days~~the two tracers over time.

simulations were driven by ERA5 reanalysis data at a horizontal resolution of 0.5° × 0.5° and 1-hourly temporal resolution. The footprints were computed differently for the $CO_2$ and $\Delta^{14}CO_2$ observations. For $CO_2$, we computed a set of footprints for each observation up to 14 days backward in time, following the approach from Monteil and Scholze (2021). Integrated $\Delta^{14}CO_2$ observations (Section 2.2) quantify the $\Delta^{14}C$ value of atmospheric $CO_2$ ~~over a period of~~ throughout 1 to 3 weeks (see Table 1). We account for this in FLEXPART by distributing the FLEXPART particles ~~release~~ released over the whole integration period of the observations. The simulations are then carried on for (up to) 14 days backward in time from the start of the integration period. A Python code was developed to run FLEXPART and post-process the footprints for being used in LUMIA (https://github.com/lumia-dev/runflex). In Figure 3, we show an example of an observation footprint for $CO_2$ and $\Delta^{14}CO_2$ at the Hyltemossa ICOS station in southern Sweden. The $CO_2$ footprint (left panel of Fig. ~~m~~ 3) shows how the observation of June 26th, 2018 at 13:00 LT is sensitive to fluxes from the North Atlantic, passing through Norway, Sweden, and finally from Sweden's East and South coasts close to the Baltic Sea. The $\Delta^{14}CO_2$ aggregated footprint, on the other hand, shows a more spread sensitivity due to the long integration time, collecting fluxes from Southern Norway, Northwestern Europe, and the Baltic.

### 3.3 Synthetic observations and background concentrations

We generate concentration time series for one year for each of the stations according to the current setup of the ICOS Atmosphere network as described in Section 2.2. For replicating the most realistic conditions of the sampling frequency, we use real sampling and integration times (in the case of radiocarbon) from the stations, taking for each one the sampling times for 2018. In this way, we account for the sampling gaps and the differences in integration times commonly produced due to ~~calibrations,~~ maintenance, and general operational eventualities. For stations with the number of observations, $\mathrm{N}_{obs}$, equal to zero in Table 1, we set fixed sampling and integration times (14 days). Most of these stations were already in operation in 2018, but some were not yet labeled as ICOS stations (e.g. Schauinsland) or had not implemented and or started the tracer measurement (e.g. ~~$\Delta^{14}\mathrm{C}$~~ $\Delta^{14}\mathrm{CO}_2$ at Ochsenkopf).

Following Monteil and Scholze (2021), we select the $\mathrm{CO}_2$ observation times according to the sampling station's elevation to guarantee the model's best representation. For sampling stations located under 1000 m.a.s.l, we select the times when the boundary layer is most likely well developed, from 11:00 to 15:00 LT. For the contrary case, we take the times around midnight, from 22:00 to 2:00 LT, where the boundary layer is most likely below the sampling intake, or in other words, is sampling the free troposphere. ~~This data selection is not strictly necessary for this study since we assume a perfect~~ For our OSSEs, we use the same transport model (~~the same model is used~~ i.e. the pre-computed observation footprints from FLEXPART) to generate the synthetic observations and perform the inversions~~). However,~~. Therefore, this data selection is not strictly necessary for this study, but we want to replicate the conditions of a real inversion. ~~We~~ Since we are using the same background concentration for the synthetic observations and the simulated prior and posterior observations (i.e. we are assuming a perfect boundary condition), we simplify the calculation of it by computing a smoothed and detrended weekly (for $\mathrm{CO}_2$) and monthly (for $\Delta^{14}\mathrm{CO}_2$) average of the real observations (ICOS et al., 2023) for each sampling site. For sampling sites, for which there are for some reason no real observations for the year 2018 in the ICOS database (e.g. $\Delta^{14}\mathrm{CO}_2$ measurements were not yet implemented or were not yet part of ICOS), we took the observations from the nearest year available to calculate the background.

We then perform a forward run of the model using the true fluxes mentioned in Section 3.1 to calculate the corresponding "true" $\mathrm{CO}_2$ and ~~$\mathrm{C}\Delta^{14}\mathrm{C}$~~ $\Delta^{14}\mathrm{CO}_2$ concentration time series and ~~then add a~~ add the background value corresponding to each site, observation time and tracer. To weaken the assumption of a perfect transport and boundary condition, we add a random perturbation to the synthetic observations~~to weaken the assumption of a perfect transport.~~. This random perturbation is equal to $y^* = y + \varepsilon \times \xi$, where $y$ is the synthetic observation, $\varepsilon$ is the observation error (both the instrumental and representativity errors, see Section 3.3.1 below), and $\xi$ is a standard normal random vector. In this way, the added perturbation is based on the observation error. Figure 4 shows the synthetic $\mathrm{CO}_2$ ~~concentration~~ and $\Delta^{14}\mathrm{CO}_2$ observation time-series and the components of each flux at Hyltemossa station. As mentioned in Section 2.1, we convert all radiocarbon values to $\mathrm{C}\Delta^{14}\mathrm{C}$ values. On the side of the observation, we do this by applying the following equation:

$$[\mathrm{C}\Delta^{14}\mathrm{C}] = \frac{[\Delta^{14}\mathrm{CO}_2] \times [\mathrm{CO}_2]}{1000} \tag{8}$$

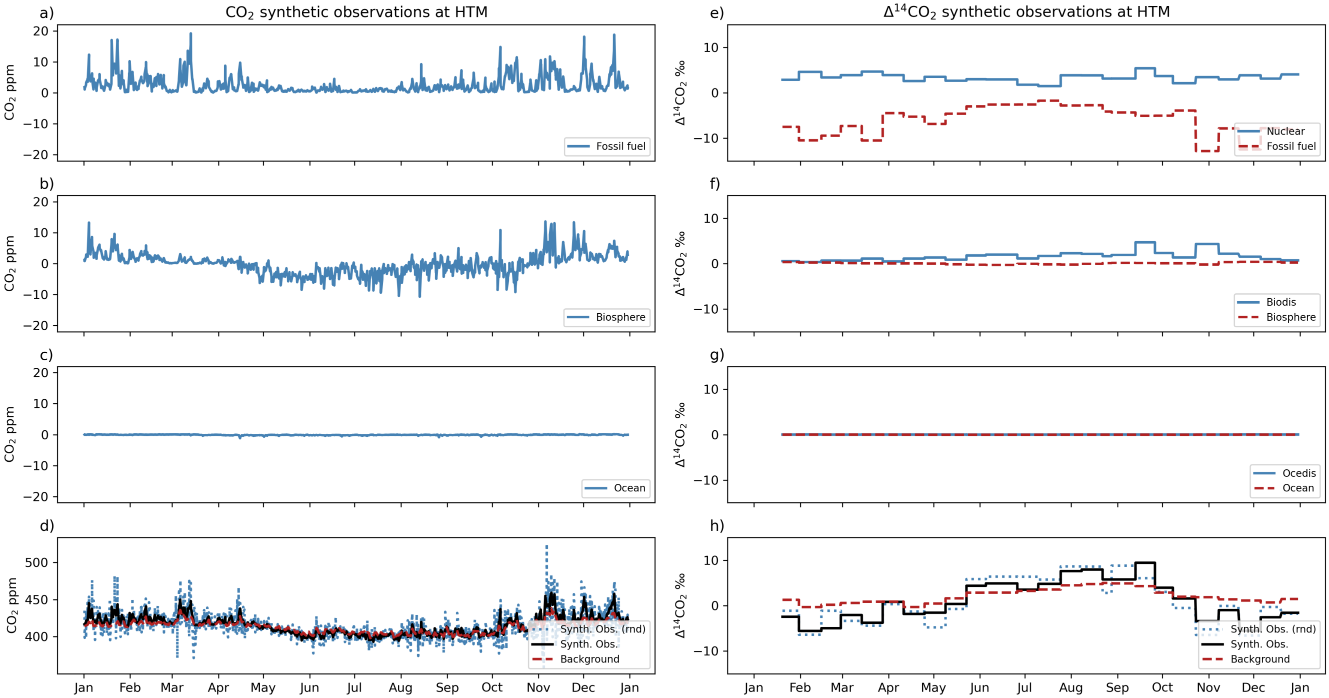

**Figure 4.** Synthetic ~~observation time-series for Hyltemossa (~~observations of $CO_2$ and $\Delta^{14}CO_2$ at the HTM ~~)~~ station over a one-year period. Panels a) to d) display $CO_2$ concentration variations due to different sources: a) fossil fuel, b) biosphere, c) ocean, and d) combined synthetic observations with random perturbation (blue dotted line) against the background concentrations (red dashed line). Panels e) to h) illustrate $\Delta^{14}CO_2$ variations: e) nuclear and fossil fuel, f) biospheric disequilibrium and biosphere, g) ocean disequilibrium and ocean, and h) total synthetic observations with random perturbation (blue dotted line) compared to the background (red dashed line). The blue solid and dashed lines represent the synthetic observations without and with random noise added, respectively.

In a real setup, this would imply having paired $CO_2$ and $\Delta^{14}CO_2$ observations, and in the case of the integrated samples, this would mean having an average of $CO_2$ observations along the integration period of the $\Delta^{14}CO_2$ sample. However, since we are using synthetic observations, we transported the $CO_2$ fluxes using the $\Delta^{14}CO_2$ footprints and stored the values to convert back and forth between $\Delta^{14}CO_2$ and $C\Delta^{14}C$ units, ‰ and ~~ppm‰~~ppm, respectively.

As can be seen from Figure 4, both $\hat{F}_{\text{oce}}$ and $\hat{F}_{\text{ocedis}}$ have virtually no impact on the concentrations at the Hyltemossa station (and all other stations used in our setup, not shown), hence we decided not to include these components in the control vector, i.e. we transport them but do not optimize them further.

### 3.3.1 Experiments and inversion setup

To make the inversions comparable, we keep the same inversion setup for all the experiments. Table 2 summarizes the main model parameter values. We choose a Gaussian horizontal correlation and an exponential temporal correlation for the prior flux uncertainties (See Section 2.3.1). Since our main purpose in this study is to demonstrate that our multi-tracer inversion system is capable of estimating both the fossil $CO_2$ emissions and natural $CO_2$ fluxes, we choose prior uncertainty values that are reasonable and consistent with other studies. The prior uncertainties are assigned as follows: ~~50% to 150% (0.1~~ for $F_{\mathrm{ff}}$, we use the difference between the annual budgets for the whole study domain from ODIAC (1.26 PgC yr$^{-1}$~~to~~) (Oda and Maksyutov, 2020) and from an emissions product based on EDGARv4.3 (1.47 PgC yr$^{-1}$) (Gerbig and Koch, 2021b) as a reference to define its uncertainty (Basu et al., 2016). We use 150% (0.3 PgC yr$^{-1}$) of the difference ~~in the annual budget (0.21~~ as the base uncertainty for all the experiments, and we select two extra values to evaluate the impact of the prescribed uncertainty on the inversion: 50% of the difference (0.1 PgC yr$^{-1}$~~) of EDGAR and ODIAC for $F_{\mathrm{ff}}$ to evaluate its impact in the inversion, 10% (0.37 PgC yr$^{-1}$~~) ~~of the annual negative values for $F_{\mathrm{bio}}$~~ and the exact difference of 0.21 PgC yr$^{-1}$ (~~where production is higher than respiration)~~ 100%). For $F_{\mathrm{bio}}$ we choose the 25% (0.37 PgC yr$^{-1}$) of the monthly prior (Monteil and Scholze, 2021), and 30% (0.22 PgC yr$^{-1}$) of the annual budget for $F_{\mathrm{biodis}}$ (Basu et al., 2020). We optimize all the categories at the same temporal resolution but at a higher horizontal resolution for $F_{\mathrm{ff}}$ and $F_{\mathrm{bio}}$ (2500 points) than for $F_{\mathrm{biodis}}$ (500 points). To set up the observation ~~uncertainty,~~ error, which includes the instrumental and the representativity errors, we use different methods for the $CO_2$ and the $\Delta^{14}CO_2$. For $CO_2$, where the error of representativity is usually larger than the instrumental error, we apply a weekly moving standard deviation to each observation i.e. the prior ~~uncertainty~~ error of each observation is equal to the standard deviation of the observations in a time window of ±3.5 days around that observation. ~~The prior uncertainty for the~~ In this way, we account for the changes in the $CO_2$ ~~observations ranges from 0.91 to 215.5 ppm~~concentrations according to the local site conditions. For instance, at a background station such as Jungfraujoch (JFJ) on the top of the Swiss Alpes, the observation error ranges from 0.9 to 29.2ppm (mean value of 9.3 ± 4.0ppm), while at polluted sites such as Saclay (SAC) just outside Paris the $CO_2$ concentrations change rapidly and the error ranges from 5.9 to 215.5ppm (mean value of 55.8 ± 40.7ppm). For $\Delta^{14}CO_2$ ~~,~~ on the other hand, the instrumental error is larger than the representativity error, we use a constant value of ~~1.5‰ for~~ 0.8ppm in C$\Delta^{14}$C units or 1.91 ± 0.05‰ in $\Delta^{14}CO_2$ units, calculated using Equation 8.

We perform one forward run and six inversions, summarized in Table 3. We generate the synthetic observations and evaluate the impact of $\hat{F}_{\mathrm{oce}}$ and $\hat{F}_{\mathrm{ocedis}}$ on the total synthetic observations as described in Section 3.3 with the forward run (SYNTH). Starting with the inversions, we perform two experiments to test the impact of having $\Delta^{14}$C observations (ZBASE and ZCO2Only). We use the prior $F_{\mathrm{ff}}$ and $F_{\mathrm{bio}}$ set to zero (both in the spatial and temporal domain) with a prior uncertainty setup based on ODIAC and VPRM, respectively. The reason to use prior fluxes set to zero is that products of both categories can have similar spatial and temporal distributions and values, making it easy for the model to retrieve the true values. Instead, we set the values to zero but give the model some information through the prior uncertainty setup. The remaining fluxes are prescribed and set to their true values. We assimilate both $CO_2$ and $\Delta^{14}$C observations for ZBASE and only $CO_2$ observations for ZCO2Only. In the second set of inversions, we use a more realistic setup. In the first, BASE, we simulate a complete and realistic inversion setup, assimilating $CO_2$ and $\Delta^{14}$C observations and optimizing $F_{\mathrm{ff}}$, $F_{\mathrm{bio}}$, and $F_{\mathrm{biodis}}$. In the BASE experiments, we change the prescribed prior uncertainty of $F_{\mathrm{ff}}$ (0.1, 0.21 and 0.3 PgC yr$^{-1}$) to evaluate its impact on the optimization. With the last inversion, BASENoBD, we evaluate the impact of the prior $F_{\mathrm{biodis}}$ product in the posterior $F_{\mathrm{ff}}$. The terrestrial disequilibrium term ($F_{\mathrm{biodis}}$) is difficult to estimate since there is a large uncertainty on the heterotrophic respiration flux and the

**Table 2.** Parameter setup used in all the inversions performed in this study.

| Fluxes | | | | | | |
|---|---|---|---|---|---|---|
| Flux category | Horizontal correlation | Temporal correlation | Prior uncertainty (PgC $yr^{-1}$) | Error structure | Optimization interval (days) | Grid points |
| $F_{\mathrm{ff}}$ | 200-g | 1-e-monthly | 0.30 | log | 7 | 2500 |
| $F_{\mathrm{bio}}$ | 500-g | 1-e-monthly | 0.37 | sqrt | 7 | 2500 |
| $F_{\mathrm{biodis}}$ | 1000-g | 2-e-monthly | 0.22 | sqrt | 7 | 500 |

| Observations | | |
|---|---|---|
| Tracer | Type of sampling | Prior uncertainty |
| $CO_2$ | Continuous 1-hour | Weekly moving standard deviation |
| $\Delta^{14}CO_2$ | Integrated 2-weekly | Constant 0.8 ppm ‰ |

**Table 3.** Inversions performed in this work.

| **Simulation** | $F_{\mathrm{ff}}$ | $F_{\mathrm{bio}}$ | $F_{\mathrm{biodis}}$ | **Optimized fluxes** | **Tracers** | **Run** |
|---|---|---|---|---|---|---|
| SYNTH | EDGAR | LPJ-GUESS | BASU | None | $CO_2$, $\Delta^{14}CO_2$ | Forward |
| ZBASE | ZEROFossil | ZEROBio | BASU | $F_{\mathrm{ff}}$, $F_{\mathrm{bio}}$ | $CO_2$, $\Delta^{14}CO_2$ | Inversion |
| ZCO2Only | ZEROFossil | ZEROBio | BASU | $F_{\mathrm{ff}}$, $F_{\mathrm{bio}}$ | $CO_2$ | Inversion |
| BASE0.1 | ODIAC | VPRM | RndBASU | $F_{\mathrm{ff}}$, $F_{\mathrm{bio}}$, $F_{\mathrm{biodis}}$ | $CO_2$, $\Delta^{14}CO_2$ | Inversion |
| ~~BASE~~ BASE0.21 | ODIAC | VPRM | RndBASU | $F_{\mathrm{ff}}$, $F_{\mathrm{bio}}$, $F_{\mathrm{biodis}}$ | $CO_2$, $\Delta^{14}CO_2$ | Inversion |
| ~~BASE0.3~~ BASE(0.3) | ODIAC | VPRM | RndBASU | $F_{\mathrm{ff}}$, $F_{\mathrm{bio}}$, $F_{\mathrm{biodis}}$ | $CO_2$, $\Delta^{14}CO_2$ | Inversion |
| BASENoBD | ODIAC | VPRM | BASU | $F_{\mathrm{ff}}$, $F_{\mathrm{bio}}$ | $CO_2$, $\Delta^{14}CO_2$ | Inversion |

age of respired carbon (Basu et al., 2016), and it may be widely different if estimated using a different vegetation model or methodology. We account for this by optimizing only the $CO_2$ fluxes, $F_{\mathrm{ff}}$ and $F_{\mathrm{bio}}$, using both $CO_2$ and $\Delta^{14}C$ observations and keeping $\hat{F}_{\mathrm{biodis}}$ prescribed.

## 4 Results

### 4.1 Impact of $F_{\mathrm{oce}}$ and $F_{\mathrm{ocedis}}$

We start by testing the impact of ocean-related fluxes ($\hat{F}_{\mathrm{oce}}$ and $\hat{F}_{\mathrm{ocedis}}$) in the total synthetic observations by performing a forward simulation (SYNTH in Table 3). Figure 4, shows the results from this forward simulation and the contribution of each flux category to the concentrations of both tracers for the Hyltemossa (HTM) station. The results show that the contribution of the ocean and ocean disequilibrium fluxes to the total concentration is below the error assigned to the synthetic observations. For $CO_2$, the average contribution is -0.07 ± 0.12 ppm (for an average observation error of 10.0 ± 5.7 ppm) at HTM, -0.07 ± 0.15 ppm (average obs. error 9.8 ± 9.0 $CO_2$ ppm) at all stations. For $\Delta^{14}CO_2$, the average contribution due to $F_{\text{oce}}$ is -0.009 ± 0.009‰ (average obs. error 1.9 ± 0.04‰) at HTM and -0.007 ± 0.007‰ (average obs. error 1.9 ± 0.05‰) at all stations. Similarly, the contribution due to $F_{\text{ocedis}}$ is 0.016 ± 0.009‰ at HTM and 0.02 ± 0.017‰ at all stations. Due to the low impact of ocean-related fluxes, we prescribe them in the inversions along with $F_{\text{nuc}}$ and optimize only $F_{\text{ff}}$, $F_{\text{bio}}$, and $F_{\text{biodis}}$. A summary for each station can be found in Appendix A.

### 4.2 Impact of adding ~~$\Delta^{14}C$~~ $\Delta^{14}CO_2$ observations

In this section, we present the results from the ZBASE and ZCO2Only experiments. We start by analyzing the retrieval of truth fossil $CO_2$ ($\hat{F}_{\text{ff}}$) and biosphere ($\hat{F}_{\text{bio}}$) time series. We divide the results into the regions shown in Figure 1, where Northern Europe represents Scandinavia, Finland, and the Baltic States, Western/Central Europe represents Benelux, France, Germany, Switzerland, Liechtenstein, and Austria, Southern Europe represents the Iberian Peninsula, Italy, and the Balkans (except for Romania and Bulgaria), Eastern Europe represents Poland, Slovakia, Hungary Romania, and Bulgaria, and the British Isles represents Ireland and the United Kingdom. The study domain includes all the land shown in Figure 1, even the countries not mentioned in the definition of the regions (countries in gray in Figure 1).

#### 4.2.1 Retrieval of the monthly and regional time series

~~The posterior fossil $CO_2$ ($F_{\text{ff}}$) time series show heterogeneous results across the regions and experiments (Figure 5) in contrast with the biosphere fluxes ($F_{\text{bio}}$), where there is , in general, a good~~ In general, there is a closer agreement between the truth and the posterior time series for the ~~two experiments in all regions (~~ZBASE and ZCO2Only experiments across all regions for the biosphere fluxes ($F_{\text{bio}}$) (Figure 6) ~~. Starting with~~ in contrast to the fossil $CO_2$ emissions ($F_{\text{ff}}$) (Figure 5). In the study domain, the ~~posterior ZBASE (adding $\Delta^{14}C$ observations ) performs better than the~~ inclusion of $\Delta^{14}CO_2$ observations in the ZBASE experiment yields better performance than ZCO2Only for both flux categories. ~~For $F_{\text{ff}}$ (Figure 5a), both experiments show a negative bias and follow the seasonality, albeit ZBASE is closer~~ Specifically, ZBASE exhibits closer alignment to the posterior ~~than ZCO2Only and therefore has a lower root mean square error (RMSE ): 1.51 TgC day$^{-1}$ versus 2.75 TgC day$^{-1}$, respectively~~ with a lower RMSE (see Table 4)~~. Posterior biosphere fluxes, on the other hand,~~ , indicating a better fit of the seasonality for $F_{\text{ff}}$. Similarly, the posterior biosphere fluxes more closely follow the true time series ~~closer than~~ than the fossil $CO_2$ emissions in both experiments, with ~~a positive bias (Figure 6a). Once again, ZBASE performs better than~~ ZBASE outperforming ZCO2Only ~~most of the year and presents smaller RMSE (ZBASE = 1.12 TgC day$^{-1}$, ZCO2Only = 2.12 TgC day$^{-1}$)~~ in terms of RMSE and BIAS values~~(ZBASE = 0.74, ZCO2Only = 1.90) (see Table 4). Before continuing with the regional results, it is important to mention the characteristics of the regions regarding the coverage of the sampling stations . In total, we consider 33 stations, all of them measuring $CO_2$ and 15 measuring additionally $\Delta^{14}C$. Most of the stations are located in~~ .

The regional analysis reflects the influence of the coverage by sampling stations on the inversion outcomes. Western/Central Europe, benefiting from the highest number of stations (18 ~~stations~~out of 33 stations considered in this study, 10 of them measuring both tracers), ~~followed by Northern Europe with eight stations, four measuring both tracers, Southern Europe with four stations measuring $CO_2$ only, the British Isles with two ($CO_2$) and Eastern Europe with one ($CO_2$ and $\Delta^{14}$C) (see Figure 1). We find the best posterior time series in Western/Central Europe, which, as we already mentioned, also has the largest number of stations. The posterior fossil $CO_2$~~ shows the best alignment between the posterior and true time series for $F_{\mathrm{ff}}$, especially in the ZBASE experiment ~~fit closely with the true time series, while ZCO2Only shows a pronounced bias~~ (Figure 5b)~~as in the case of the study domain for both experiments. Likewise, the posterior biosphere shows better results when adding $\Delta^{14}$C observations (ZBASE)than without them (ZCO2Only), in which the latter has a positive bias most of the year (Figure 6b). Eastern Europe~~ , while ZCO2Only shows pronounced RMSE and BIAS values (Table 4). Conversely, regions like Eastern Europe (one station measuring both tracers) and the British Isles ~~show a posterior ZBASE fossil~~ (two stations measuring only $CO_2$~~close to the truth despite their low coverageof sampling stations. Eastern Europe shows the best results during the year for ZBASE, and ZCO2Only follows the tendency from the last regions (Figure 5d). The British Isles show a posterior ZBASE fossil $CO_2$ with more differences from~~), despite their lower station coverage, exhibit posterior ZBASE $F_{\mathrm{ff}}$ time series that closely approximate the truth, ~~particularly at the beginning of the year , where the posterior surpasses the truth in almost 100% of its value(Figure 5f), resulting in a similar RMSE but a lower BIAS than ZCO2Only (Table 4)~~with Eastern Europe showing consistent performance throughout the year (panels d and f in Figure 5). However, the posterior ZBASE biosphere fluxes in these ~~two~~ regions do not ~~show a good fit to the truth as~~ align as closely with the true values as observed in e.g. Western/Central Europe (panels d and f in Figure 6). In Eastern Europe, the posterior ZBASE shows big differences with the truth during May, June (maximum difference of 0.42 TgC day$^{-1}$), and later in September, while ZCO2Only shows a better fit during these months but a positive bias the rest of the year (Figure 6d). In contrast, the posterior biosphere flux from the ZCO2Only experiment shows a better fit to the truth than the ZBASE one in the British Isles (Table 4). ~~The ZBASE experiment shows a negative bias most of the year, except from March to May (Figure 6f).~~

Lastly, Southern and Northern Europe show similar results despite their differences: Northern Europe has better coverage of sampling stations, and its annual truth fossil $CO_2$ emissions are lower (an average of 0.20 TgC day$^{-1}$ against 0.59 TgC day$^{-1}$). In both regions, the posterior ~~fossil $CO_2$~~ $F_{\mathrm{ff}}$ of the two experiments is far from the truth (Figures 5c and 5e)~~. The posterior biosphere~~ , while the posterior $F_{\mathrm{bio}}$ of both regions and experiments is close to each other, with Northern Europe showing a better fit to the truth than Southern Europe, in which the posterior shows a more pronounced positive bias along the year (Figures 6c and 6e).

### 4.2.2 Analysis of the spatial error reduction

We set up the ZBASE and ZCO2Only experiments with prior uncertainties and error structures as in Table 2 based on the values of ODIAC for $F_{\mathrm{ff}}$ and VPRM for $F_{\mathrm{bio}}$. Therefore, the model had some information about the spatial and temporal error structure of the prior fluxes. To evaluate the spatial performance of LUMIA, we ~~calculate pixel-level annual total prior~~ first aggregate the hourly values (both truth and posterior) to the optimization interval of one week. After this, we calculate the

**Table 4.** RMSE and BIAS values for $F_{\mathrm{ff}}$ and $F_{\mathrm{bio}}$ from the ZBASE and ZCO2Only experiments in all the regions.

| **Region** | **Fossil fuel ($F_{\mathrm{ff}}$)** | | | | | | **Biosphere ($F_{\mathrm{bio}}$)** | | | | | |
|---|---|---|---|---|---|---|---|---|---|---|---|---|
| | **RMSE (TgC day^-1)** | | | **BIAS** | | | **RMSE (TgC day^-1)** | | | **BIAS** | | |
| | **Prior** | **ZBASE** | **ZCO2Only** | **Prior** | **ZBASE** | **ZCO2Only** | **Prior** | **ZBASE** | **ZCO2Only** | **Prior** | **ZBASE** | **ZCO2Only** |
| Study Domain | 4.07 | 1.51 | 2.75 | -4.03 | -1.51 | -2.74 | 4.66 | 1.12 | 2.12 | 1.18 | 0.74 | 1.90 |
| Western/Central Europe | 1.26 | 0.12 | 0.53 | -1.25 | -0.06 | -0.52 | 0.97 | 0.17 | 0.46 | 0.15 | -0.04 | 0.43 |
| Southern Europe | 0.60 | 0.42 | 0.51 | -0.59 | -0.41 | -0.50 | 0.89 | 0.35 | 0.41 | 0.35 | 0.29 | 0.35 |
| Eastern Europe | 0.55 | 0.07 | 0.33 | -0.54 | -0.02 | -0.33 | 0.61 | 0.22 | 0.34 | 0.15 | -0.04 | 0.26 |
| Northern Europe | 0.20 | 0.19 | 0.20 | -0.20 | -0.19 | -0.20 | 0.76 | 0.21 | 0.25 | 0.00 | 0.16 | 0.22 |
| British Isles | 0.28 | 0.14 | 0.15 | -0.28 | 0.07 | -0.21 | 0.30 | 0.16 | 0.09 | 0.02 | -0.13 | -0.02 |

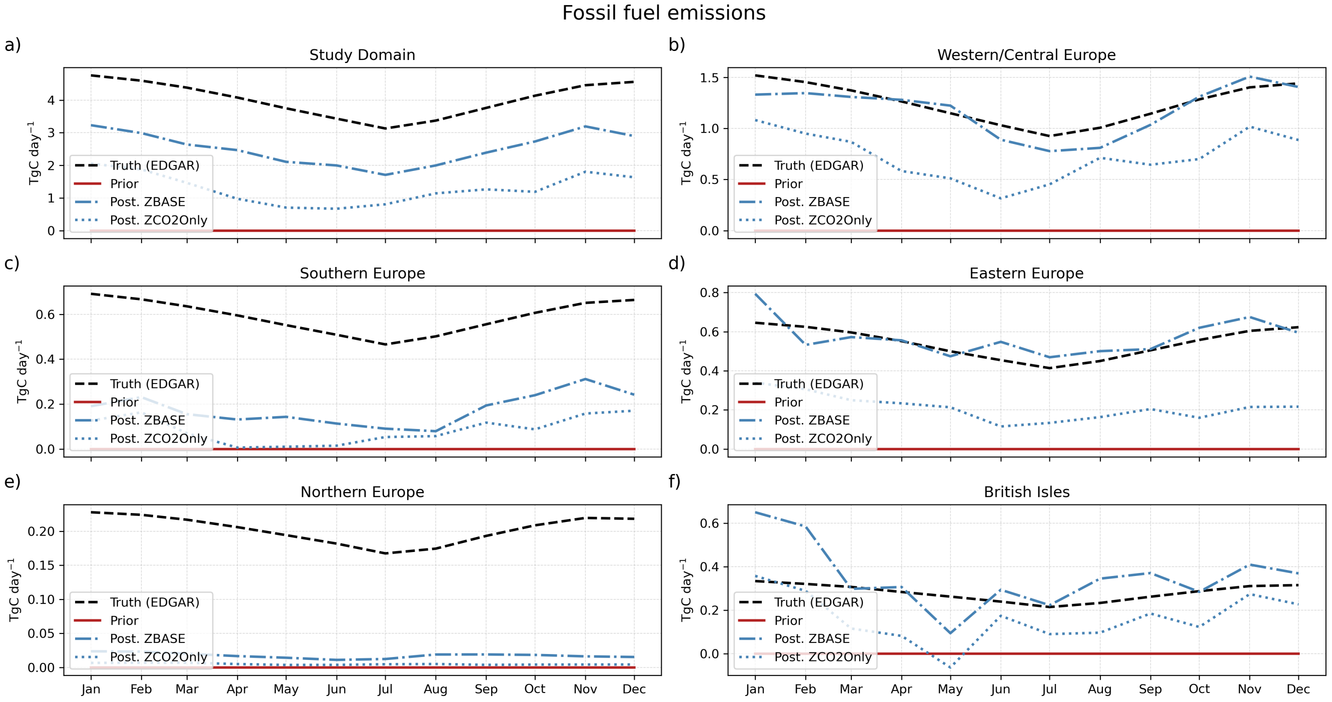

**Figure 5.** Monthly fossil $CO_2$ truth (dashed lines), prior (solid lines), and posterior fluxes from the ZBASE (dashed-dotted lines) and ZCO2Only (dotted lines) experiments for a) the study domain and the 5 sub-regions defined: b) Western/Central Europe, c) Southern Europe, d) Eastern Europe, e) Northern Europe, and f) British Isles.

posterior RMSE of each experiment and flux category ~~(fossil and biosphere) and the relative RMSE reduction comparing the two experiments for each flux category (Figure 7) defined as~~ at the grid cell level, and finally, we calculate the RMSE reduction by subtracting the posterior RMSE of ZBASE from the posterior RMSE of ZCO2Only as follows:

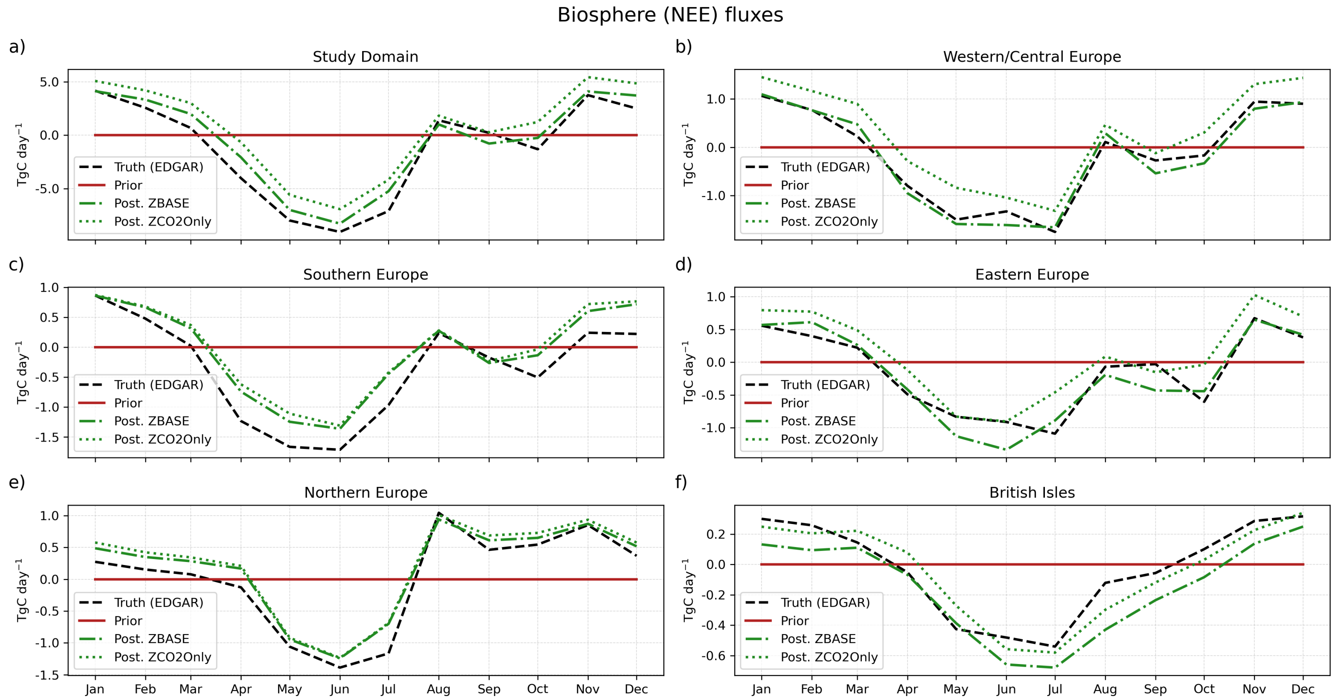

**Figure 6.** Monthly biosphere (NEE) truth (dashed lines), prior (solid lines), and posterior fluxes from the ZBASE (dashed-dotted lines) and ZCO2Only (dotted lines) experiments for a) the study domain and the 5 sub-regions defined: b) Western/Central Europe, c) Southern Europe, d) Eastern Europe, e) Northern Europe, and f) British Isles.

$$RMSE_{\text{reduction}} = ((RMSE^{apos}_{\text{ZCO2Only}} - RMSE^{apos}_{\text{ZBASE}}) - \mu)/\sigma \tag{9}$$

~~where $\mu$ is the average value of the difference between the two RMSEs and $\sigma$ its standard deviation.~~ Here, positive values of $RMSE_{\text{reduction}}$ indicate posterior $RMSE^{apos}_{\text{ZBASE}}$ values that are lower than $RMSE^{apos}_{\text{ZCO2Only}}$, i.e. ~~pixels~~ grid cells where when adding $\Delta^{14}C$ observations (ZBASE) shows values closer to the truth (better performance, lower RMSE) than when only having $CO_2$ observations (ZCO2Only). ~~Since the prior here is zero, the prior RMSE maps (Figures 7a and 7c) show the locations where fluxes have their larger values (either negative or positive for biosphere) during the year.~~ For fossil fuel, we find ~~higher~~ larger prior RMSE values in Western/Central Europe, but as well some ~~pixels~~ grid cells show the location of larger cities like in southern England, Poland, and Spain (Figure 7a). For the biosphere fluxes, we find the ~~stronger~~ larger prior RMSE values in Western/Central Europe and the British Isles (Figures 7~~c~~e).

The largest positive RMSE reductions (where ZBASE performs better than ZCO2Only) (Figures 7~~b and 7d) occurs~~ d and 7h) occur around the sampling stations in Western/Central Europe and the British Isles for both flux categories. For fossil $CO_2$, most of the study domain has positive values (92%), although a large part of these values (around 75%) is close to zero, representing the values in Southern and Northern Europe where there is a low adjustment of the fluxes when adding $\Delta^{14}C$

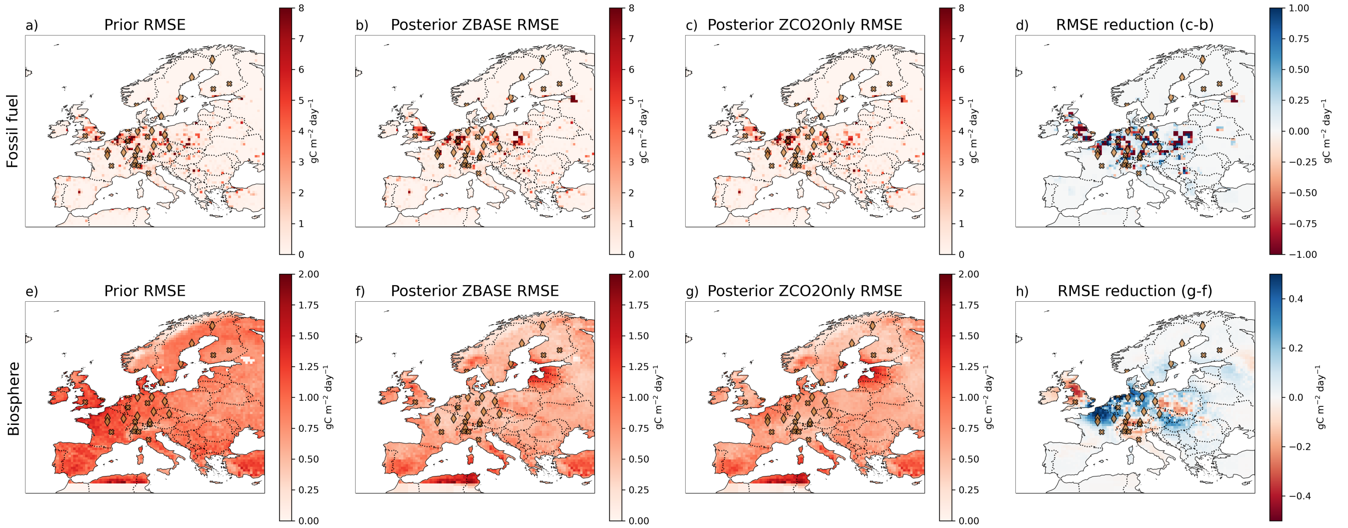

**Figure 7.** Spatial error of fossil $CO_2$ (a to d) and biosphere (e to h) for the ZBASE and ZCO2Only experiments. a) and ~~e~~e) show the prior RMSE for $F_{\mathrm{ff}}$ and $F_{\mathrm{bio}}$, respectively, ~~and~~ b) and f) show the posterior RMSE for ZBASE, c) and g) show the posterior RMSE for ZCO2Only, and d) and h) show the ~~relative~~ RMSE reduction (see Equation 9) for fossil and biosphere. In Figures ~~b~~d) and ~~d~~h), positive values (in blue) show the pixels where ZBASE performs better than ZCO2Only (i.e. adding ~~$\Delta^{14}C$~~ $\Delta^{14}CO_2$ observations improves the posterior estimates), and negative values (in red) where ZCO2Only performs better than ZBASE. Crosses and diamonds represent stations that only measure $CO_2$ and those that additionally measure ~~$\Delta^{14}C$~~$\Delta^{14}CO_2$, respectively.

observations (Figure 7~~b~~d). For the biosphere fluxes, ~~despite~~ the posterior RMSE maps (Figures 7f and 7g) show the regions that are poorly constrained due to the absence of observations such as the southern part of the domain and the Baltic States. Despite a lower portion of the study domain (40%) (Figure 7h) is showing an improvement in the posterior estimation when adding $\Delta^{14}$C observations compared with fossil fuel, this presents a clearer pattern in areas such as southeast England, the northern part of Western/Central Europe, Denmark, and southern Sweden, as well as some areas in Eastern Europe.

### 4.2.3 Recovery of the annual budget

Next, we assess how accurately the model can estimate the annual budget for fossil fuel, biosphere (NEE), and the total $CO_2$. Figure 8 shows the annual budget of the study domain, the sub-regions (right), and some of the largest European countries by area (left). We include the ODIAC emission ~~inventory~~ data product and the VPRM product for the biosphere in Figure 8 as references since we base the prior uncertainty and error structure on the spatial and temporal distribution of these two products. As we find in the temporal distribution (Figure 5), in the study domain, the posterior fossil $CO_2$ from both experiments does not fit the truth, but ZBASE shows a lower bias from the truth than ZCO2Only. This result is reflected in the annual budget, where ZBASE recovers 63% from $\hat{F}_{\mathrm{ff}}$ while ZCO2Only recovers only 32% (Figure 8a). Likewise, the posterior $F_{\mathrm{bio}}$ of ZBASE that closely fits $\hat{F}_{\mathrm{bio}}$, recovers 38% of the biosphere budget (Figure 8b), while ZCO2Only, which shows a larger positive bias in the temporal distribution, returns a positive annual budget, contrary to the negative annual budget of the true biosphere fluxes. This behavior is repeated in most of the regions and countries shown in Figure 8, where ZCO2Only strongly underestimates the annual fossil $CO_2$ emissions, with the lowest estimates in Southern (15%) and Northern Europe (2%), the latter with a strong underestimation from ZBASE as well (9%), France (33%), and Spain ($\sim$ 0%), which has a similar situation as Northern Europe (5% recovery for ZBASE), and returns an annual biosphere budget that compensates for the total $CO_2$ budget which is close to ZBASE in most of the cases.

Western and Eastern Europe show the best posterior $F_{\mathrm{ff}}$ ZBASE values, 95%, and 105% of the truth, respectively. However, while some countries in these regions with good sampling coverage, such as the Benelux Union, show good recovery of $\hat{F}_{\mathrm{ff}}$ (96%), some others with fewer neighboring sampling stations, such as France and Poland, show results far from the annual fossil $CO_2$ emissions: 71% and 166%, respectively. Germany, which has the best coverage in the study domain, shows some overestimation (111%). On the other hand, the biosphere annual budget compensates in most cases for the total $CO_2$ budget, returning values that over and underestimate the truth, where the only regions with closer values are Western/Central Europe (126%) and Eastern Europe (128%) for the ZBASE experiment (Figure 8c). Finally, we find better estimates of the total $CO_2$ budget in most cases for the ZBASE experiment, with the largest recovery in Western/Central Europe (91%), Eastern Europe (96%), and Northern Europe (89%) (Figure 8e), and in the country level in Germany (99%) and France (94%) (Figure 8f).

### 4.3 A realistic setup

The most realistic approach we can take to perform OSSEs is to use a realistic set of prior fluxes that differ substantially from the true fluxes used to generate the synthetic observations. In this section, we perform a series of experiments using the prior $F_{\mathrm{ff}}$, $F_{\mathrm{bio}}$, and $F_{\mathrm{biodis}}$ fluxes described in Section 3.1 to evaluate the impact of prescribing different prior fossil $CO_2$ uncertainty values as well as the impact of the prior $F_{\mathrm{biodis}}$ flux product (RndBASU) in the optimization of $F_{\mathrm{ff}}$.

#### 4.3.1 Impact of the prior fossil $CO_2$ uncertainty

Figure 9 shows the weekly $F_{\mathrm{ff}}$ time series for the three experiments using different prior uncertainties (BASE0.1, ~~BASE~~BASE0.21, and BASE0.3). The EDGAR ($\hat{F}_{\mathrm{ff}}$) and ODIAC (prior) products have different temporal distributions along the year, with ODIAC being flatter than EDGAR, but both with a minimum during summer, for EDGAR in July (3.13 TgC day$^{-1}$), and for ODIAC in August (3.05 TgC day$^{-1}$). In the study domain (Figure 9a), the posterior $F_{\mathrm{ff}}$ for the three experiments is very close to each other and approaches the truth from January to February and later from August to December. From May to August, there is an increment in the posterior fluxes that depart from $\hat{F}_{\mathrm{ff}}$ ~~, and~~ with the maximum difference in July that we find in Western/Central Europe (~~Figure 9b) and to a greater extent~~ ranging from 0.10 for BASE0.1 to 0.17 TgC day$^{-1}$ for BASE0.3) and in Eastern Europe ~~, particularly for BASE0.3 (Figure 9d). All~~ (0.08 to 0.26 TgC day$^{-1}$) (Figure 9). The posterior time series from the three experiments have the same RMSE with respect to the truth, 0.48 TgC day$^{-1}$, which is lower than the prior RMSE of 0.65 TgC day$^{-1}$. The posterior $F_{\mathrm{ff}}$ time series in Western/Central Europe shows the best results, with the estimates being close to truth, except for June and July. The three experiments show the same performance, reducing the RMSE by 50% ($\mathrm{RMSE_{prior}}$ = 0.26 TgC day$^{-1}$, $\mathrm{RMSE_{BASE0.1}}$ = 0.13 TgC day$^{-1}$), but ~~BASE~~ BASE0.21 and BASE0.3 show the values farther

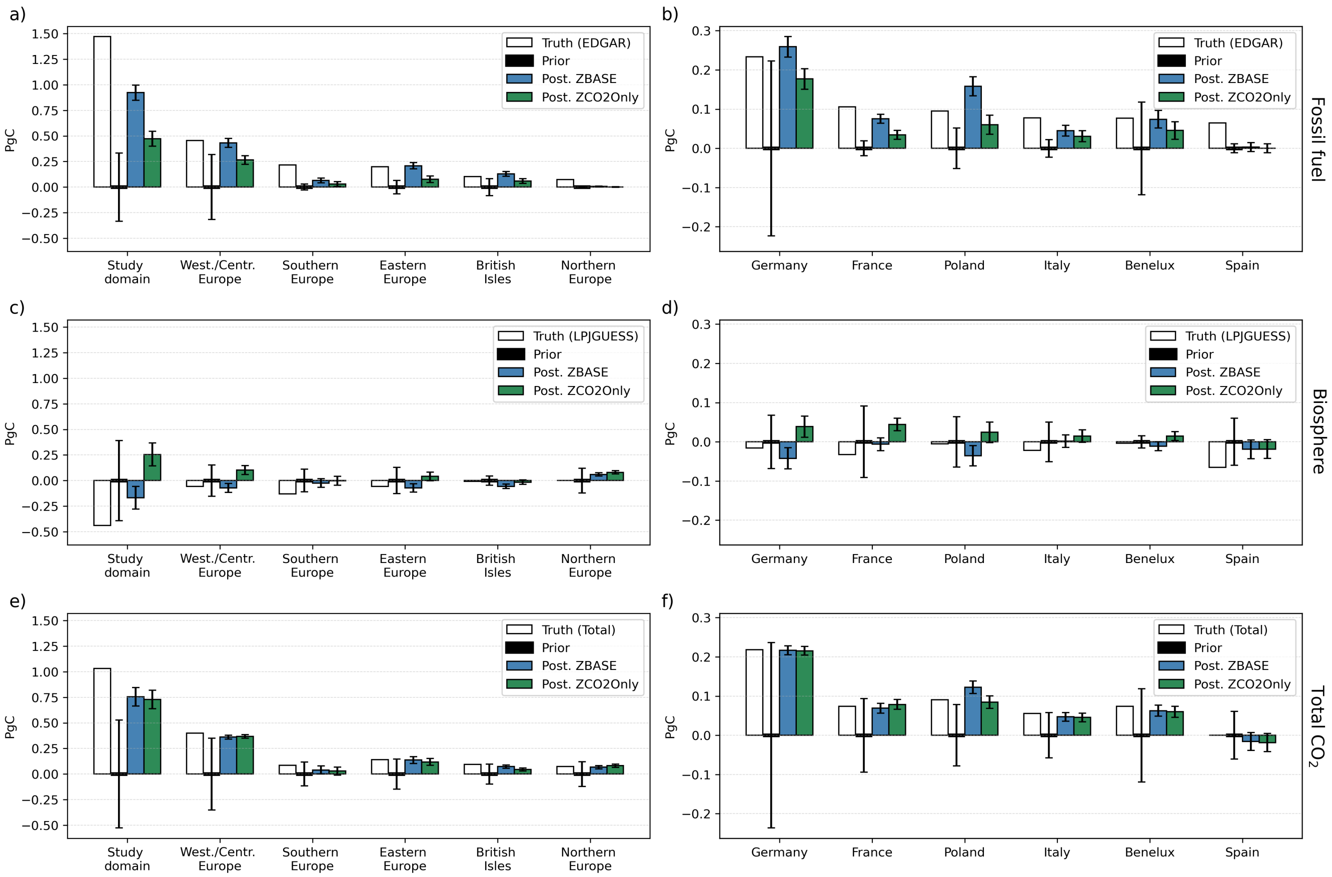

**Figure 8.** ~~Annual~~ True, prior and posterior annual budgets of fossil (a-b), biosphere (c-d) and total $CO_2$ (e-f) for the study domain, the sub-regions (right), and some of the largest European countries by area (left). The white bars show the true ~~emissions~~ annual budgets based on ~~the~~ EDGAR ~~emission inventory~~and LPJ-GUESS flux products. The ~~red~~ black bars ~~(horizontal hatching) are for reference and~~ represent ~~fluxes according to~~ the ~~ODIAC for fossil $CO_2$ (a and b)~~prior value, ~~VPRM for biosphere (c and d), and the sum of the two for total $CO_2$ (e and f)~~0 PgC. The blue ~~, green,~~ and ~~gray~~ green bars show the posterior ~~fossil fuel, biosphere, and total $CO_2$ fluxes for the~~ budgets of ZBASE ~~(grid hatching)~~ and ZCO2Only~~(diagonal hatching) experiments~~, respectively. The ~~red line represents~~ error bars represent the prior ~~value, 0 PgC~~and posterior uncertainty calculated with a Monte Carlo ensemble of 100 members.

from the truth in June and July. Northern Europe (Figure 9c), on the other hand, shows priors that are already very close to the truth, with a posterior RMSE equal to the truth of 0.07 TgC day$^{-1}$. Finally, in Eastern Europe, with the lowest sampling coverage, the three posterior time series degrade the prior estimate.

The difference in the annual budget of EDGAR and ODIAC for the study domain is 0.21 PgC for the year 2018, which is as large as the emission of the country with the largest emission in the study domain for the same year, Germany, with 0.23 PgC according to EDGAR, and 0.19 PgC according to ODIAC (Figure 10). This difference in the study domain is nearly recovered

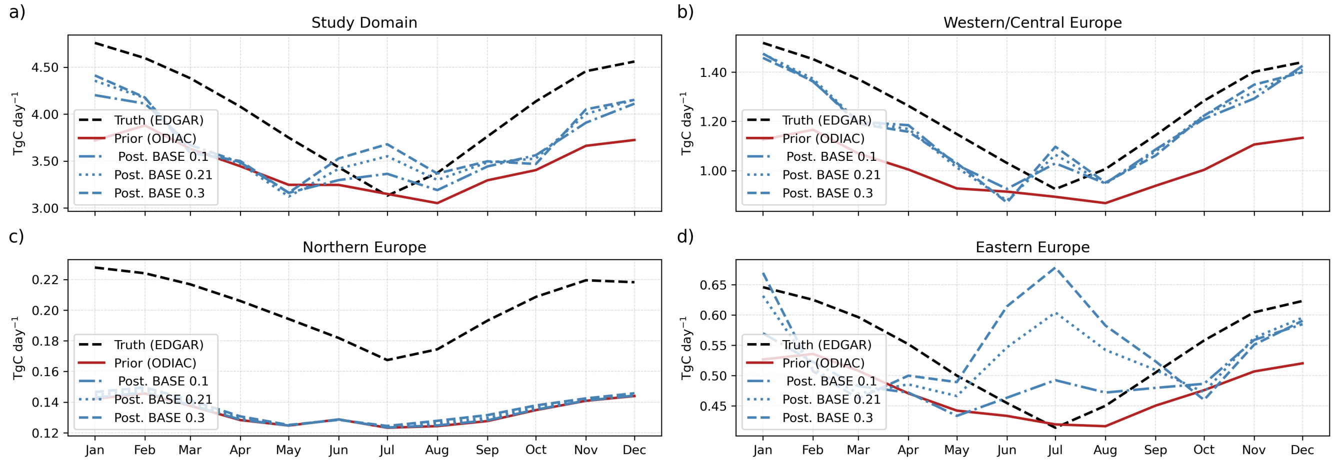

**Figure 9.** Monthly fossil $CO_2$ truth (black dashed lines), prior (red solid lines), and posterior fluxes from the BASE0.1 (blue dashed-dotted lines), BASE0.21 (blue dotted lines), and BASE0.3 (blue dashed lines) experiments for a) the study domain and the 3 sub-regions: b) Western/Central Europe, c) Northern Europe, and d) Eastern Europe (note the different scales on the y-axis).

by all three experiments, with a recovery ranging from 30% for BASE0.1 to 45% for BASE0.3~~having the highest recovery, 92%~~. In Western/Central Europe, the three experiments recover 96% of the truth (around 71% of the difference between true and prior), similar to Germany, where the recovery ranges from 94% for BASE0.1 to 97% for BASE0.3 (68% to 82% of the difference). As we find in the time series (Figure 9d), the prior annual budget is very close to the truth both in Eastern Europe, where the difference is 0.02 PgC, and in Poland, 0.01 PgC. In both cases, the posterior recovers the annual budget, with ~~overestimations~~ overestimation from BASE0.3 for the whole ~~region and from BASE~~ sub-region and from BASE0.21 and BASE0.3 in Poland, which are as big as 120%. Finally, and as expected from Figure 9c and the prior uncertainty for the sub-region, there is no recovery of the annual budget in Northern Europe further than the prior estimate.

### 4.3.2 Impact of the terrestrial isotopic disequilibrium product

The prior $F_{\mathrm{bio}}$ and $F_{\mathrm{biodis}}$ are very different in magnitude from the true values, with differences as large as 13.4 TgC day$^{-1}$ and 7.6 TgC day$^{-1}$, respectively, during summer for the whole study domain (Figures 11d and 11g). This gap is well resolved for $F_{\mathrm{bio}}$ in the study domain and Western/Central Europe (Figures 11d and 11f), and with some underestimation in Eastern Europe between June and September (Figure 11e). However, for the posterior $F_{\mathrm{biodis}}$ we find some larger differences from the truth during June and September in the study domain and the two sub-regions. When we prescribe $F_{\mathrm{biodis}}$ (BASENoBD), the posterior $F_{\mathrm{ff}}$ values from June to August in the study domain and Western/Central Europe (Figures 11a and 11b) get closer to $\hat{F}_{\mathrm{ff}}$, and after the summer in the study domain. This can also be seen in an improvement in the RMSE values with 0.32 TgC day$^{-1}$ for the study domain and 0.10 TgC day$^{-1}$ for Western/Central Europe. In Eastern Europe, the posterior $F_{\mathrm{ff}}$ for

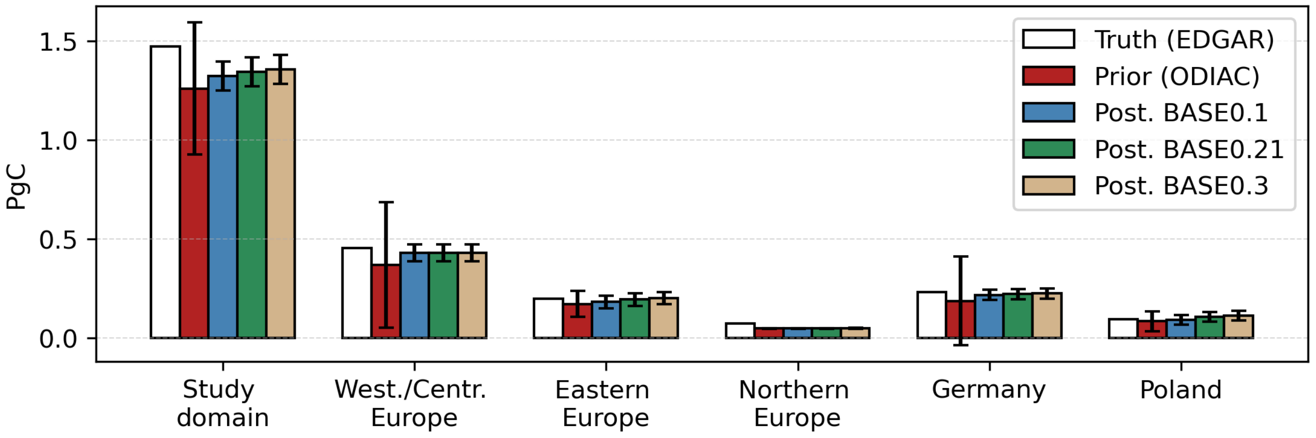

**Figure 10.** Total annual fossil $CO_2$ emissions for the study domain, Western/Central Europe, Eastern Europe, Northern Europe, Germany, and Poland. The white bars show the true emissions based on the EDGAR emission ~~inventory~~database. The red bars show the prior fluxes based on the ODIAC ~~emissions inventory~~emission data product. The blue, green and tan bars show the posterior fossil $CO_2$ emissions for the BASE0.1~~(grid hatching)~~, BASE0.21~~(diagonal hatching)~~, and BASE0.3 ~~(cross hatching)~~ experiments, respectively. The error bars represent the prior and posterior uncertainty calculated with a Monte Carlo ensemble of 100 members.

**Table 5.** Performance metrics (correlation coefficient R, standard deviation and $\chi^2$) for all sites, Saclay (SAC), and Jungfraujoch (JFJ).

| | | **Prior** | | **Posterior** | |
|---|---|---|---|---|---|
| | | R | $\sigma$ | R | $\sigma$ |
| All sites | $CO_2$ | 0.64 | 14.2 | 0.68 | 13.4 |
| | $\Delta^{14}CO_2$ | 0.72 | 6.4 | 0.99 | 1.2 |
| SAC | $CO_2$ | 0.56 | 31.9 | 0.59 | 31.1 |
| | $\Delta^{14}CO_2$ | 0.63 | 6.8 | 0.99 | 0.5 |
| JFJ | $CO_2$ | 0.65 | 5.5 | 0.74 | 4.5 |
| | $\Delta^{14}CO_2$ | 0.75 | 4.2 | 0.84 | 1.5 |
| | $\chi^2$ | 1.77 | | 1.06 | |

BASENoBD experiments does not show a significant improvement and, on the contrary, further degrades the prior estimate during the summer and the autumn.

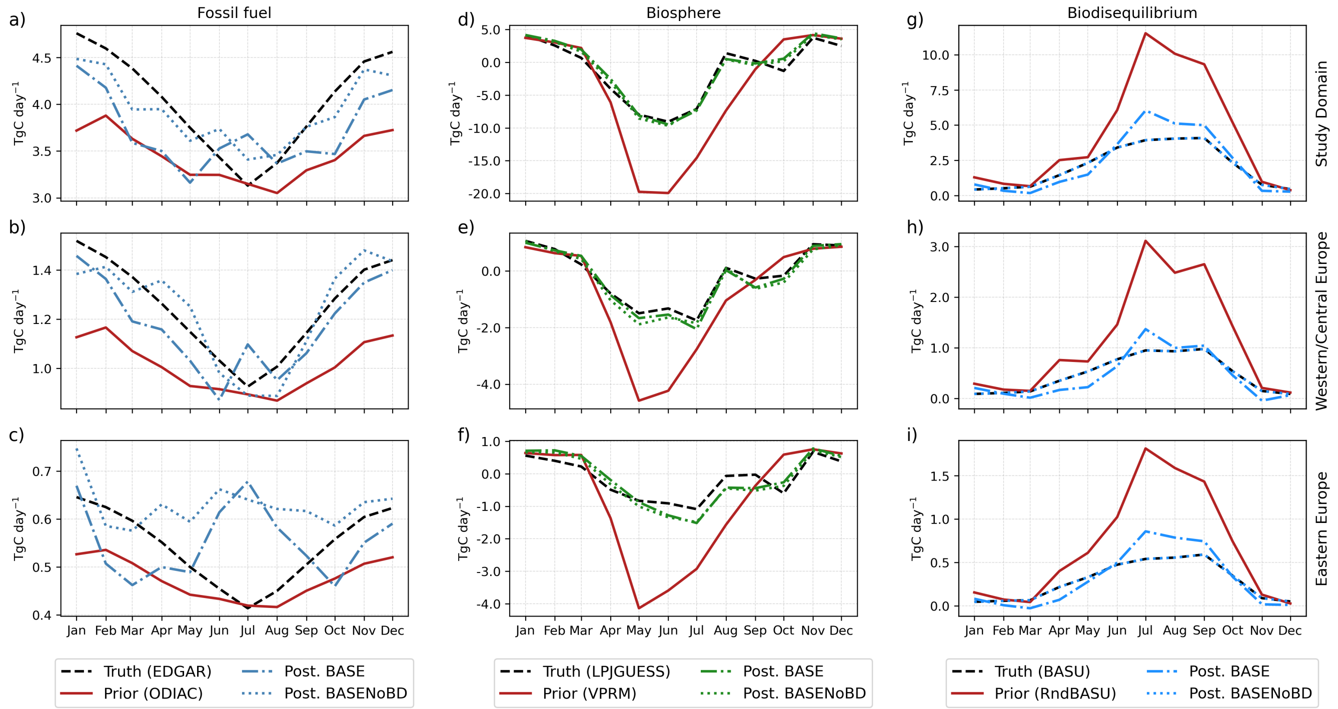

**Figure 11.** Monthly time series of $F_{\mathrm{ff}}$ (a) to c)), $F_{\mathrm{bio}}$ (d) to f)), and $F_{\mathrm{biodis}}$ (g) to i)), for the study domain (top panel), Western/Central Europe (center panel), and Eastern Europe (bottom panel). The truth is represented in black dashed lines, prior in red solid lines, ~~and~~ posterior fluxes from the BASE0.1 in blue dashed-dotted lines, and BASENoBD in blue dotted lines.

### 4.3.3 The observational space

Finally, we analyze the model's performance in the observational space ~~, which is crucial for evaluating its effectiveness. Figure 12compares the prior and posterior concentrations from the BASE0.1 experimentwith the corresponding synthetic observations for all sampling stations and , as a representative example, for the Jungfraujoch (JFJ)station. Examining the correlation coefficients, we find that the prior concentrations already correlate significantly with the synthetic observations . The correlation coefficients for the prior estimates are 0.61 for JFJ~~ at all sampling stations aggregated together, one polluted station (Saclay, SAC) (Figure 12) and one background station (Jungfraujoch, JFJ) (Figures 12 and 13) for the BASE experiment. We calculate two performance metrics: the correlation coefficient between the synthetic observations and the prior and posterior simulated concentrations for all the sites and individually for the two sites selected, and the $\chi^2$ for the overall simulation (Table 5). The histograms in Figure 12 show the mismatches between the synthetic observations and the prior and posterior concentrations. For the $CO_2$ concentrations at all sites (Figure 12~~b)and 0.92 (Figure 12~~a)~~for all stations, indicating a reasonable correlation with the synthetic observations~~, the histogram shows a distribution centered around zero for both prior and posterior mismatches with a standard deviation of 14.2 and 13.4, respectively (see Table 5), indicating systematic deviations from the

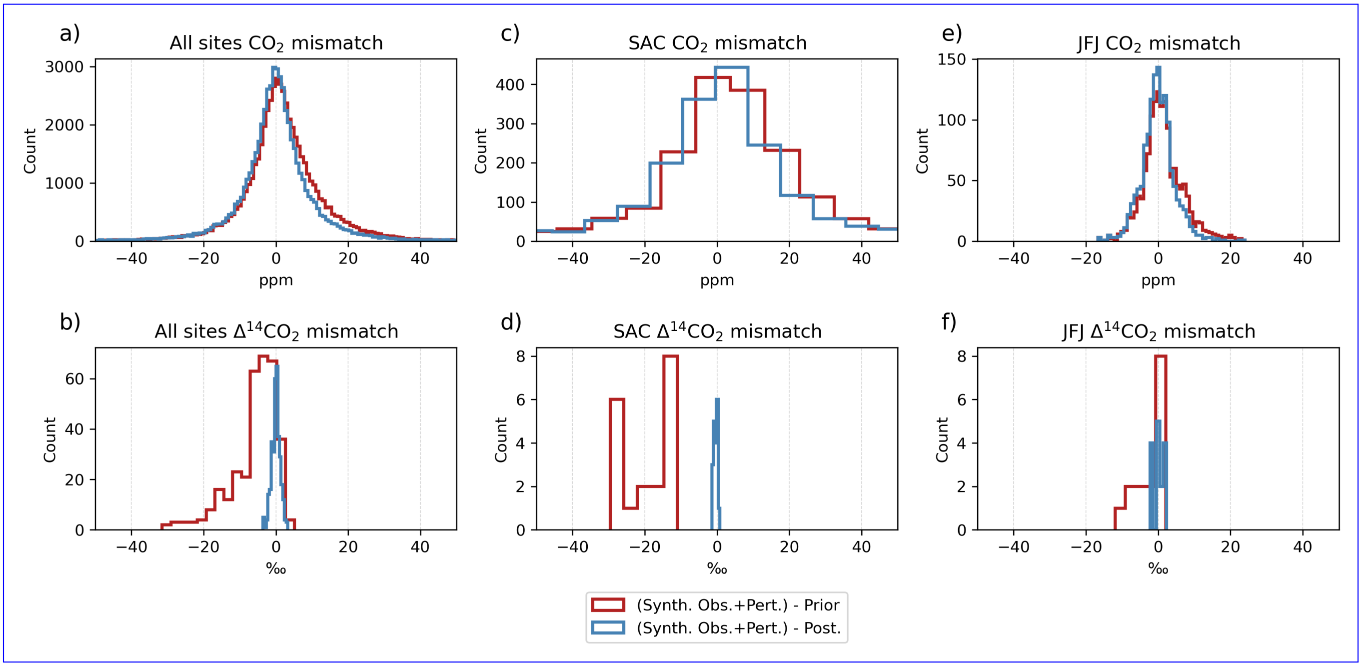

**Figure 12.** Mismatches between the synthetic observations and the prior (red) and posterior (blue) concentrations for all the sampling stations, Saclay (SAC) and Jungfraujoch (JFJ) for $CO_2$ (a, c and e) and for $\Delta^{14}CO_2$ (b, d and f). All prior and posterior concentrations correspond to the BASE experiment.

observed values. The posterior mismatch has a slightly tighter distribution, suggesting a small improvement in the model after adjustments as reflected in the correlation coefficient (Table 5). At Saclay (Figure 12c), the mismatch distribution is wider than the aggregate of all sites, which could suggest greater variability or larger errors at this particular site. The posterior adjustment has not significantly tightened the distribution, indicating that the model adjustments did not perform as well at this site as they did on average across all sites. On the other hand, the ~~posterior concentrations exhibit a slight enhancement in the correlation coefficients compared to the prior concentrations: 0.71 for JFJ (Figure 12b) and 0.98 (Figure 12c)for all stations, indicating a refinement in the model's ability to reproduce the synthetic observations accurately. This improvement in correlation coefficients is also reflected in the mismatch plots. For example, the mismatch between the posterior concentrations and the synthetic observations of $\Delta^{14}C$ at all stations~~ distribution in Jungfraujoch (Figure 12e) is much tighter than in all sites and SAC, with the posterior mismatch displaying a slight improvement in precision as evidenced by the narrower spread. However, when comparing the posterior time series with the synthetic observations before adding the random perturbation (Figures 13a and 13c), there is a better agreement between them than with the prior values, especially during periods of higher variability (April to July at SAC, and April to September at JFJ).

The $\Delta^{14}CO_2$ synthetic observations are in general better fitted by the posterior than $CO_2$ at all sites, SAC and JFJ (Table 5). In all cases, the prior distribution is displaced to the negative values, indicating that the prior simulated values are in general higher than the synthetic observations as shown for the whole period at SAC (Figure 12~~c) shows a narrower distribution around zero compared to the previous mismatch. This suggests that the inversion process has effectively adjusted the model outputs, bringing them closer to the true observations. Analyzing the concentration time series at the JFJ station~~ d) and from July to November at JFJ (Figure 12f). These larger prior concentrations are mainly caused by the prior terrestrial disequilibrium flux from July to November, and by the nuclear production fluxes throughout the year, which is significantly larger at Saclay (Figure 14). However, the posterior mismatches showed a much narrower spread around zero at all sites (Figure 12~~e and~~ b), Saclay (Figure 12d), and Jungfraujoch (Figure 12f) ~~, we observe that~~ that is evident in the time series at both sites where the posterior closely follows the ~~posterior concentrations agree better with the~~ synthetic observations~~than the prior concentrations. This improvement is particularly notable for $\Delta^{14}$C, indicating that the inversion has successfully captured the dynamics of this tracer. Lastly, we consider the~~ , and supported by the correlation coefficients (Table 5).

The reported $\chi^2$ values of 1.77 for the prior and ~~posterior concentrations across all sampling stations and observations. The prior~~ 1.06 for the posterior across all sites and samples suggest a substantial improvement in the model's performance in adjusting the prior concentrations to the synthetic observations. A $\chi^2$ ~~value is 1.52, indicating some discrepancy~~ of 1.77 for the prior indicates that there were significant discrepancies between the prior ~~concentrations~~ and the synthetic observations. ~~However, the posterior~~ This is consistent with the broader spread of mismatches in the histograms for both SAC and JFJ sites, as well as the apparent overestimation of $\Delta^{14}CO_2$ content in the time series. The improvement to a $\chi^2$ ~~value improves to 1.00, indicating a closer match between the posterior concentrations and the observed data. These results confirm that the inversion process has effectively improved the model's performance in the observational space.~~ of 1.06 for the posterior indicates a better fit to the synthetic observations that are likely to be reflective of the underlying data patterns while still maintaining some degree of generalizability without overfitting the data.

## 5 Discussion

Under the current sampling strategy and observation network, we demonstrate through OSSEs that adding $\Delta^{14}CO_2$ observations can help us constrain fossil $CO_2$ emissions over Europe using the LUMIA system. We start with two simulation experiments in which we set the prior fossil $CO_2$ and biosphere (Net Ecosystem Exchange, NEE) ~~flux~~ fluxes to zero: ZBASE and ZCO2Only. ~~Since~~ Under an OSSE setup, even when using completely different truth and prior flux products (~~truth and prior)can have similar spatial and temporal distributions in an OSSE setup, it can be~~ e.g. different spatiotemporal distributions and annual budgets), due to assumptions such as a perfect transport model and background concentrations, it is easy for the model to retrieve the true values even without adding $\Delta^{14}CO_2$ observations. For this reason, we set up these two ~~experiments in a very challenging way for the model~~ more challenging experiments to assess the capabilities of the ~~model~~ inversion system to constrain the fossil $CO_2$ emissions and ~~the~~ biosphere fluxes using $CO_2$ and $\Delta^{14}CO_2$. The ZBASE and ZCO2Only experiments show us that in regions with a dense sampling network, such as Western/Central Europe, when adding $\Delta^{14}CO_2$ observations, LUMIA is capable of recovering the seasonality of $F_{\mathrm{ff}}$ and $F_{\mathrm{bio}}$~~(Figures 5 and 6)~~, as well as the total annual $CO_2$ budget ~~(Figure 8)~~ of the whole region and some of the larger countries (also in terms of fossil $CO_2$ emissions) such as Germany and France. On

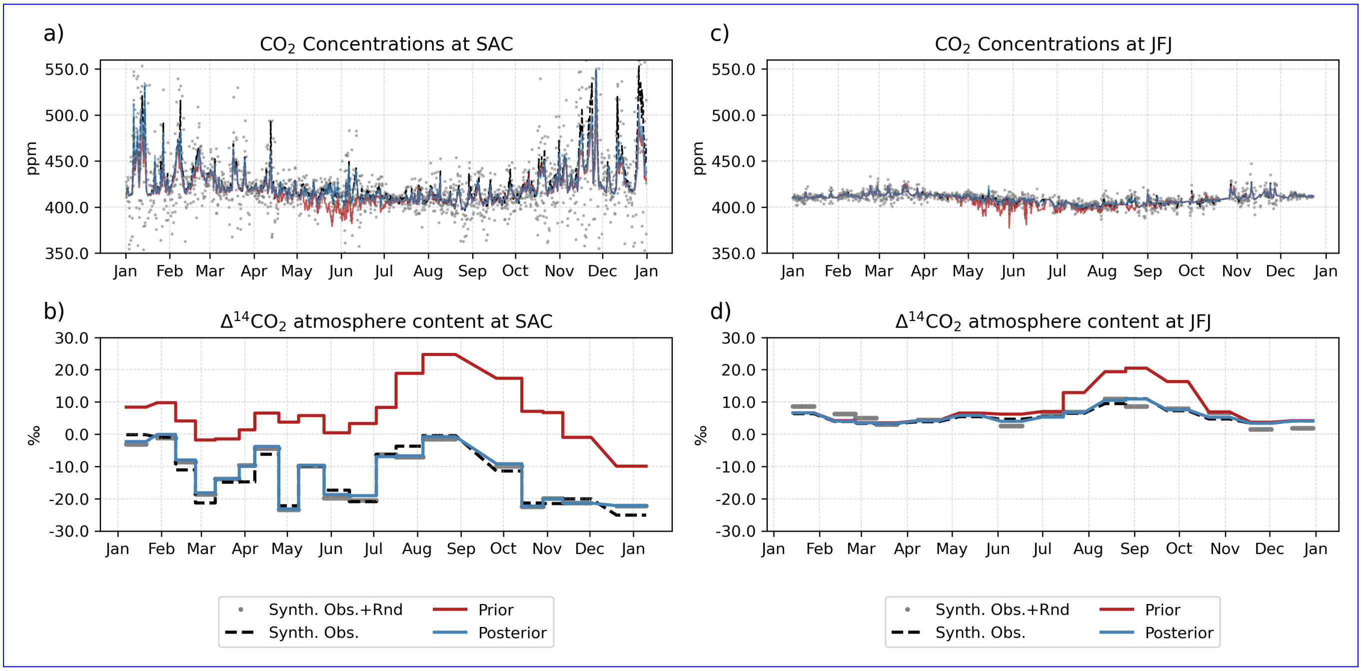

**Figure 13.** ~~Mismatches between the synthetic observations and the prior (red) and posterior (blue) concentrations for all the sampling stations and at Jungfraujoch ICOS station for~~ Concentration time series of CO$_2$ (a and ~~b~~c) and ~~for Δ$^{14}$C~~ Δ$^{14}$CO$_2$ (~~c~~ b and d) ~~. The right panel shows the time series of CO$_2$~~ at Saclay (~~e~~SAC) and ~~Δ$^{14}$C~~ Jungfraujoch (~~f~~JFJ)~~at Jungfraujoch~~, respectively. All prior and posterior concentrations correspond to the ~~BASE0.1~~ BASE experiment.

the other hand, the results in Northern Europe, which has a relatively good network coverage, ~~does not show as good results as~~ are not as good as in Western/Central Europe ~~in the case of~~ regarding fossil CO$_2$. Comparing the ranges of the true fossil CO$_2$ and biosphere fluxes in Northern and Western/Central Europe, we find that, while $\hat{F}_{\text{bio}}$ has a similar range in both regions~~(-2.22 to 1.47 TgC day$^{-1}$ in Northern Europe and -2.26 to 1.21 TgC day$^{-1}$ in Western/Central Europe)~~, $\hat{F}_{\text{ff}}$ differs by one order of magnitude~~: 0.16 to 0.23 1.47 TgC day$^{-1}$ in Northern Europe and 0.91 to 1.52 TgC day$^{-1}$ in Western/Central Europe~~. Using the concept of signal-to-noise ratio, if we consider the fossil CO$_2$ as the signal (the variable in which we are more interested) and the biosphere as the noise, this difference of one order of magnitude between them in Northern Europe makes it easier for the model to recover the biosphere fluxes than the fossil CO$_2$ emissions, even with additional information about ~~Δ$^{14}$C.~~

~~This situation is also clear in the study domain and the other regions. The terrestrial biosphere flux (NEE) exhibits a large seasonal pattern that provides a strong enough signal from the inversion to generate this temporal pattern in the posterior $F_{\text{bio}}$ for the whole study domain and the sub-regions (Figure 6) for both experiments, despite the bias that we find in most of~~ Δ$^{14}$CO$_2$. In addition, the prior uncertainty which is proportional to the ~~regions. However, the fossil CO$_2$ seasonality is not as strong as the NEE on a regional scale, and with poor sampling coverage and no information about Δ$^{14}$C, it is impossible for the model to retrieve the seasonality of the~~ fluxes, is close to zero for the fossil fluxes, while it is two orders of magnitude larger for

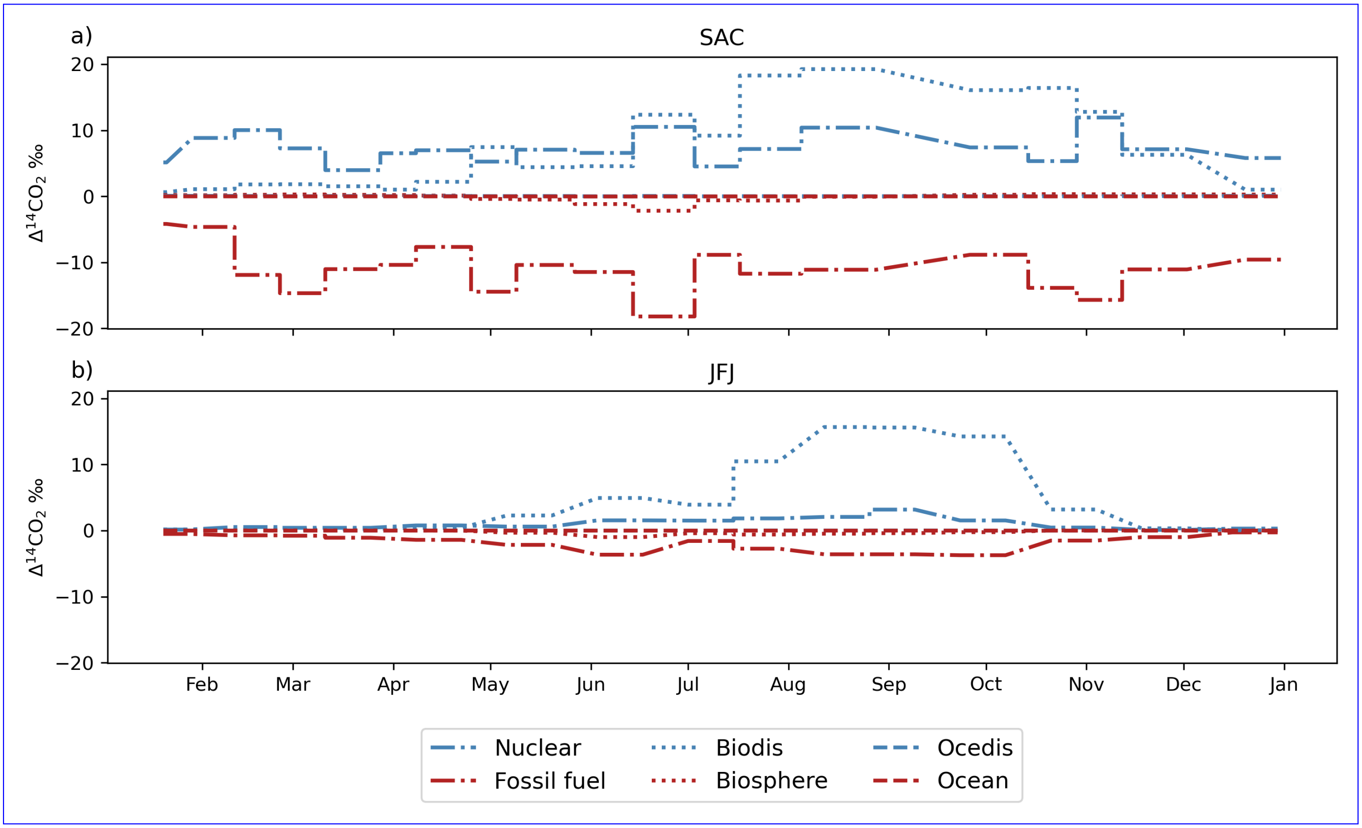

**Figure 14.** Contribution of each category to the prior $\Delta^{14}CO_2$ simulated concentrations at Saclay (a) and Jungfraujoch (b).

the biosphere, making it for the inversion more costly to constrain the fossil $CO_2$ emissions~~in regions such as Southern Europe, Eastern Europe, and the British Isles. These results are confirmed by the BASE experiments, in which inversions improve the posterior fossil $CO_2$ time series (Figure 10) and annual budget (Figures 9d and 11), but not in regions lacking observations , such as Eastern Europe~~ .

~~Wang et al. (2018) found similar results in Europe despite large~~ The inversions are able to resolve the NEE both at the continental level and in the sub-regions but struggle more with fossil emissions in some regions with few observations (e.g. Southern Europe and the British Isles). This is similar to what was found by Wang et al. (2018) despite the differences between their inversion implementation and our LUMIA system. The main differences lie in the transport model and the inversion approach. They use a global transport model at a resolution of $3.75° \times 2.5°$ (Laboratoire de Météorologie Dynamique's LMDZv4) and a ~~precalculated~~ pre-calculated fossil $CO_2$ tracer (product of the mass balance), while we use a Lagrangian regional transport model at a higher horizontal resolution ($0.5° \times 0.5°$) and optimize both the fossil and the natural fluxes using as tracers $CO_2$ and $\Delta^{14}CO_2$. Wang et al. (2018) found the largest error reductions around Germany, Benelux, and eastern France, where most sampling stations are located. Northern Europe was also poorly constrained in ~~their~~ its inversions, similar to what we find. Wang et al. (2018) attributed the results in Northern Europe to the coarse spatial resolution of the transport model. But even with a higher resolution transport model as employed in LUMIA, we ~~can still~~ still can not resolve the true fossil $CO_2$ emissions in an OSSE setup given the current $CO_2$ and $\Delta^{14}CO_2$ observation networks. ~~A~~ We think that a more likely explanation is the difference in the magnitude of the fossil $CO_2$ emissions in ~~the~~ this region against the natural fluxes~~and other regions. A workaround can be the normalization~~. This can be seen by the differences in the seasonal amplitude of the fluxes~~or the implementation of regional scaling factors that allow having similar magnitudes across the study domain but still, the impact from other sources of noise, such as the background concentration (boundary condition) , which includes the fluxes transported from other regions within the domain, can make it difficult to solve~~. In Western/Central Europe $F_{\mathrm{bio}}$ and $F_{\mathrm{ff}}$ are of a similar order of magnitude (2.81 TgC day$^{-1}$ for $F_{\mathrm{bio}}$ and 0.6 TgC day$^{-1}$ for $F_{\mathrm{ff}}$) (see Figures 5 and 6). In contrast, in Northern Europe, there is a tenfold difference in the seasonal amplitude of the two fluxes: 2.44 TgC day$^{-1}$ for $F_{\mathrm{bio}}$ and 0.06 TgC day$^{-1}$ for $F_{\mathrm{ff}}$. In addition, the prior uncertainty for $F_{\mathrm{ff}}$ (0.002 PgC year$^{-1}$) in this region is much lower compared to $F_{\mathrm{bio}}$ (0.12 PgC year$^{-1}$) in Northern Europe.

The ~~realistic approach shows us~~ BASE experiments, in which we use realistic prior fluxes, show that the posterior fossil $CO_2$ emissions are not very sensitive to the prescribed prior uncertainty in regions with a dense sampling network~~. This is a positive result since the prior uncertainty is difficult to define both in magnitude and in spatial and temporal structure. Basu et al. (2016), for example, defined the prior uncertainty as the inter-prior spread (i.e. the difference among multiple prior~~, even when using a low prior $F_{\mathrm{ff}}$ uncertainty in which case it is more difficult for the inversion algorithm to recover the true fluxes. As we have observed in previous studies using LUMIA (Monteil et al., 2020; Monteil and Scholze, 2021), the cost of fitting the observations dominates the total cost function value. In this sense, the relative value of the prior uncertainty of $F_{\mathrm{bio}}$ against $F_{\mathrm{ff}}$ ~~products), and as they pointed out in the study, this inter-prior spread is comparable in magnitude with the annual average NEE estimated by CarbonTracker~~is going to significantly impact the spatio-temporal distribution of flux adjustments, but the total uncertainty of the fluxes is of lesser importance since the model has enough freedom to adjust the data. In other words, the error structure and how is it set up for the different flux categories, is going to have more impact than the total prior uncertainty. Both Basu et al. (2016) and Wang et al. (2018) highlight the importance of a regional horizontal correlation and error structure for fossil $CO_2$ emissions. In ~~this~~ our study, we use the same horizontal correlation and error structures developed by Monteil et al. (2020) originally for NEE. We are aware of the necessity of defining specific structures for fossil $CO_2$ within LUMIA due to the low improvement in spatial terms that we find in Figure 7 when adding $\Delta^{14}CO_2$ observations. However, it is important to mention that given the sparse observation network, we can expect spatial misattributions (flux corrections that should happen in one place but are instead made elsewhere), and therefore, we should interpret the results aggregated at the scale that is relevant given the model setup, as we demonstrate through the time series and annual budget results. Such spatial misattribution is illustrated in the spatial RMSE reduction results for the biosphere fluxes. We can clearly identify the formation of dipoles (clusters of larger RMSE values) in regions with no observations such as the southern part of the study domain and the Baltic States indicating that these areas are underconstrained.

We also find the prior terrestrial disequilibrium product to have an important impact on the posterior fossil $CO_2$ emissions (Figure 11). The prior terrestrial isotopic disequilibrium flux in our experiments is on purpose incorrect with the aim of showing the impact that it can have in the estimation of fossil $CO_2$ emissions. As shown in Figure 11, the maximum difference between the prior and the true $F_{\mathrm{biodis}}$ is of the same order of magnitude for Western/Central Europe (2.1 TgC day$^{-1}$) and Eastern Europe (1.3 TgC day$^{-1}$) in July. For $F_{\mathrm{ff}}$, however, the difference between the prior and truth is about one order of magnitude larger for Western/Central Europe compared to Eastern Europe (0.03 vs 0.005 TgC day$^{-1}$). This larger difference causes a stronger dilution of the fossil emissions in Eastern Europe, and therefore essentially lowers the signal-to-noise ratio of the $\Delta^{14}\mathrm{CO}_2$ measurements, and added to the lower network coverage compared to Western/Central Europe, a poorer constrain of the fossil $\mathrm{CO}_2$ emissions. According to Turnbull et al. (2009), one of the main contributors to atmospheric $\Delta^{14}\mathrm{CO}_2$ is heterotrophic respiration in natural environments. Therefore, having a good prior $F_{\mathrm{biodis}}$ estimate is crucial in estimating posterior $F_{\mathrm{ff}}$. The impact of $F_{\mathrm{biodis}}$ and the other $\Delta^{14}\mathrm{CO}_2$ flux terms is not negligible~~and will be explored in a follow-up study. Particularly,~~, particularly, the emissions from nuclear facilities that can have a larger impact than the terrestrial disequilibrium (Graven and Gruber, 2011) as was evident when analyzing the individual impacts of the flux categories, showing that at sampling sites heavily influenced by emissions from nuclear facilities such as Saclay, these emissions can be as large as the terrestrial isotopic disequilibrium fluxes. In this study, we fixed the $F_{\mathrm{nuc}}$ term (i.e. we use the same fluxes for calculating the synthetic observations and in the inversions), and hence, its impact is not considered here. ~~However, available information about radiocarbon emissions from nuclear facilities is only available annually (Graven and Gruber, 2011; Zazzeri et al., 2018) that are usually distributed constantly throughout the year, while in reality, nuclear facilities have routine gas releases during periodic purges and venting~~In previous studies (Wang et al., 2018; Basu et al., 2016, 2020) the $F_{\mathrm{nuc}}$ is usually prescribed and assumed as an annual value at each nuclear facility location (Graven and Gruber, 2011; Zazzeri et al., 2018) due to a lack of knowledge on the temporal distribution of these emissions. This variability in nuclear emissions has been only studied by measuring the atmospheric content of $\Delta^{14}\mathrm{CO}_2$ in the surrounding areas of single nuclear ~~power plant~~ facilities (Turnbull et al., 2014; Vogel et al., 2013; Lehmuskoski et al., 2021), but not yet in a large regional setup, and therefore it needs further investigation.

The Observing System Simulation Experiment (OSSE) framework used in this study assumes a perfect realization of atmospheric transport and mixing processes by employing the same transport model across the simulations. This assumption simplifies the complex nature of atmospheric dynamics and is a common approach to limit the scope of variability in such studies. However, it is crucial to acknowledge that this simplification overlooks one of the largest sources of uncertainty in atmospheric inverse modeling: the accurate representation of atmospheric transport and mixing processes. The variability and uncertainty in atmospheric transport can significantly impact the estimation of greenhouse gas sources and sinks. As demonstrated by Schuh et al. (2019), inconsistencies in transport simulations can introduce systematic biases in surface flux estimations, which can be as substantial as 1.7 PgC year$^{-1}$ for large zonal bands. In a study by Munassar et al. (2023), in which multiple combinations of global and regional models were tested using two different inversion frameworks (LUMIA and CarboScope-Regional (CSR)), they found that using a different regional transport (FLEXPART and STILT (Stochastic Time-Inverted Lagrangian Transport)) model can cause differences in the posterior NEE annual budget of 0.51 PgC year$^{-1}$. This highlights the sensitivity of inversion-derived emission estimates to the accuracy of the transport model used and emphasizes the critical role that transport uncertainty plays across global flux inversion systems.

Furthermore, the assumption of perfect boundary conditions in the model presents another significant simplification. Boundary conditions in atmospheric modeling can greatly influence the concentration gradients and flux estimates, and their mischaracterization can propagate errors throughout the model domain. Coming back to the study by Munassar et al. (2023), the use of a different global transport model (TM3 and TM5) for the estimation of the boundary condition can cause discrepancies in the posterior annual budget as large as 0.23 PgC year$^{-1}$. Errors in these aspects of the transport model could lead to skewed emission estimates. Given these considerations, the presented results should be interpreted with caution, understanding that the true uncertainty in atmospheric inverse modeling is likely understated in these OSSEs. It underscores the need for more comprehensive approaches that account for transport model uncertainties, such as employing ensemble modeling techniques that incorporate multiple transport models and boundary conditions to better capture the inherent uncertainties in atmospheric dynamics (Locatelli et al., 2015; Aleksankina et al., 2018).

## 6 Conclusions and future perspectives

We have expanded the LUMIA system to be capable of simultaneously inverting atmospheric observations of $CO_2$ and $\Delta^{14}CO_2$ to estimate fossil $CO_2$ emissions and net terrestrial biosphere $CO_2$ fluxes over Europe. We performed the first observing system simulation experiments to test the performance of the $\Delta^{14}C$-enhanced LUMIA version. In the first set of experiments, we show the impact of adding $\Delta^{14}C$ observations in a scenario with prior estimates of $F_{\mathrm{ff}}$ and $F_{\mathrm{bio}}$ set to zero. In regions with good sampling network coverage, assimilating both $CO_2$ and $\Delta^{14}C$ observations allows recovering the seasonality of $F_{\mathrm{ff}}$ and $F_{\mathrm{bio}}$ and the annual $F_{\mathrm{ff}}$ budget, while when assimilating only $CO_2$ observations, the posterior $F_{\mathrm{ff}}$ is degraded. In the second set of experiments, we performed ~~OSSES~~ OSSEs using more realistic priors to test the impact of the prescribed $F_{\mathrm{ff}}$ uncertainty and the impact of the prior $F_{\mathrm{biodis}}$ product. The prescribed prior uncertainty has no significant impact on the posterior $F_{\mathrm{ff}}$. On the other hand, the prior $F_{\mathrm{biodis}}$ product can significantly impact the posterior $F_{\mathrm{ff}}$.

~~In future work , we will revisit the~~ The purpose of this study is to describe the multi-tracer, more specifically $CO_2$ and $\Delta^{14}CO_2$, version of LUMIA and illustrate its application to estimate both fossil $CO_2$ emissions natural $CO_2$ fluxes simultaneously. Future work should analyze in more detail the impact of various aspects of our inversion set-up here, such as the assumption of a perfect transport model, the specification of the boundary conditions as well as different spatiotemporal error structures, on the posterior fossil $CO_2$ emissions and natural $CO_2$ fluxes. Particular emphasis should be placed on the analysis of the impact of the prior $F_{\mathrm{biodis}}$ product using simulated terrestrial biosphere disequilibrium estimates by, e.g. the LPJ model following the methodology by Scholze et al. (2003) ~~. We will also evaluate~~ because our study here illustrated the importance of this flux term in the $CO_2$ and $\Delta^{14}CO_2$ inversion. In addition, the impact of the prior $F_{\mathrm{nuc}}$, the sampling strategy, and the network density of the $\Delta^{14}C$ observations on the capability to estimate fossil $CO_2$ emissions needs to be evaluated. The current 2-weekly integrated sampling strategy allows us to get a reasonable estimate of the annual budget over the whole domain. But the inversion can neither recover the correct temporal behavior nor the spatial distribution of the fossil $CO_2$ ~~emission~~ emissions when using $C\Delta^{14}C$ observations provided by the current 2-weekly integrated sampling strategy. Additionally, converting ~~$\Delta^{14}C$~~ $\Delta^{14}CO_2$ values to $C\Delta^{14}C$ implies calculating the average of the $CO_2$ observations during the 2-week integration period that can introduce additional errors that we did not account for in this study. We will evaluate the use of hourly flask samples under different strategies as described by Levin et al. (2020), such as a "smart" sampling based on pollution episodes of $CO_2$ and CO. This will be in preparation for the intensive ~~$\Delta^{14}C$~~ $\Delta^{14}CO_2$ sampling campaign (hourly samples taken every third day) planned within the EC's Horizon Europe CORSO (CO2MVS Research on Supplementary Observations) project (https://corso-project.eu/) during 2024 at 10 ICOS stations located in Western Europe.

*Code availability.* The LUMIA source code used in this paper has been published on Zenodo and can be accessed at https://doi.org/10.5281/zenodo.8426217.

*Data availability.* The revised EDGARv4.3 https://doi.org/10.18160/GFNT-5Y47, LPJ-GUESS https://doi.org/10.18160/p52c-1qjm, and VPRM https://doi.org/10.18160/VX78-HVA1 datasets are availabale from the ICOS-Carbon Portal. ODIAC data is available at https://doi.org/10.17595/20170411.001. The input data has been uploaded on Figshare and is available at https://doi.org/10.6084/m9.figshare.24307162.

## Appendix A: Summary of ocean and ocean disequilibrium-derived synthetic observations

**Table A1.**

| Station | Ocean | Ocean | Ocedis | Synth. Obs. | Synth. Obs. (rnd) | Obs. Error | Synth. Obs. | Synth. Obs. (rnd) | Obs. Error |
|---|---|---|---|---|---|---|---|---|---|
| | CO$_2$ ppm | $\Delta^{14}$C ‰ | $\Delta^{14}$C ‰ | CO$_2$ ppm | CO$_2$ ppm | CO$_2$ ppm | $\Delta^{14}$C ‰ | $\Delta^{14}$C ‰ | $\Delta^{14}$C ‰ |
| All sites | -0.07 ± 0.15 | -0.007 ± 0.007 | 0.02 ± 0.017 | 414.6 ± 12.7 | 414.6 ± 18.3 | 9.8 ± 9.0 | 0.3 ± 8.0 | 0.2 ± 8.4 | 1.9 ± 0.05 |
| GAT | -0.07 ± 0.1 | -0.008 ± 0.007 | 0.021 ± 0.014 | 415.7 ± 12.7 | 416.2 ± 19.2 | 11.1 ± 7.2 | 2.1 ± 4.2 | 2.6 ± 4.8 | 1.9 ± 0.05 |
| HPB | -0.04 ± 0.05 | -0.005 ± 0.003 | 0.016 ± 0.008 | 414.0 ± 11.2 | 414.5 ± 16.7 | 10.4 ± 6.3 | 1.0 ± 6.3 | 1.5 ± 6.8 | 1.9 ± 0.04 |
| HTM | -0.07 ± 0.12 | -0.009 ± 0.009 | 0.016 ± 0.009 | 415.4 ± 12.3 | 415.5 ± 16.8 | 10.0 ± 5.7 | 1.0 ± 4.5 | 0.5 ± 4.8 | 1.9 ± 0.04 |
| JFJ | -0.03 ± 0.04 | -0.002 ± 0.002 | 0.01 ± 0.005 | 409.1 ± 5.0 | 409.0 ± 6.9 | 4.2 ± 2.1 | 5.5 ± 2.3 | 5.5 ± 2.9 | 2.0 ± 0.02 |
| KIT | -0.06 ± 0.06 | -0.005 ± 0.004 | 0.024 ± 0.012 | 427.1 ± 16.9 | 427.4 ± 26.9 | 17.7 ± 10.0 | -5.2 ± 10.5 | -4.7 ± 11.0 | 1.9 ± 0.05 |
| KRE | -0.05 ± 0.06 | -0.005 ± 0.004 | 0.014 ± 0.009 | 415.3 ± 12.6 | 415.0 ± 16.9 | 10.3 ± 6.0 | -4.0 ± 4.6 | -4.2 ± 4.9 | 1.9 ± 0.05 |
| LIN | -0.06 ± 0.09 | -0.007 ± 0.006 | 0.017 ± 0.011 | 420.9 ± 16.9 | 420.2 ± 25.2 | 15.2 ± 11.6 | -7.7 ± 9.4 | -8.2 ± 9.5 | 1.9 ± 0.05 |
| NOR | -0.07 ± 0.14 | -0.009 ± 0.009 | 0.011 ± 0.01 | 415.8 ± 10.7 | 415.5 ± 14.4 | 8.5 ± 4.8 | 4.9 ± 4.3 | 4.5 ± 5.1 | 1.9 ± 0.03 |
| OPE | -0.07 ± 0.08 | -0.006 ± 0.004 | 0.034 ± 0.021 | 416.7 ± 14.3 | 416.5 ± 21.5 | 13.3 ± 9.3 | -1.6 ± 6.8 | -1.2 ± 6.3 | 1.9 ± 0.04 |
| OXK | -0.06 ± 0.08 | -0.006 ± 0.004 | 0.02 ± 0.013 | 411.0 ± 7.3 | 410.8 ± 10.5 | 7.1 ± 3.0 | 1.8 ± 4.8 | 1.5 ± 5.8 | 1.9 ± 0.03 |
| PAL | -0.1 ± 0.13 | -0.011 ± 0.007 | 0.005 ± 0.004 | 412.3 ± 8.6 | 412.3 ± 10.8 | 6.0 ± 3.7 | 8.7 ± 4.2 | 8.9 ± 5.0 | 1.9 ± 0.03 |
| SAC | -0.08 ± 0.1 | -0.009 ± 0.007 | 0.04 ± 0.02 | 425.2 ± 23.0 | 425.6 ± 37.9 | 23.1 ± 20.0 | -13.1 ± 8.3 | -13.7 ± 8.8 | 1.9 ± 0.03 |
| STE | -0.08 ± 0.12 | -0.01 ± 0.007 | 0.021 ± 0.01 | 413.4 ± 10.0 | 413.7 ± 15.6 | 9.4 ± 7.2 | 0.4 ± 4.9 | -0.4 ± 6.2 | 1.9 ± 0.03 |
| SVB | -0.1 ± 0.16 | -0.011 ± 0.009 | 0.007 ± 0.006 | 412.5 ± 9.5 | 412.0 ± 12.4 | 7.1 ± 4.5 | 5.8 ± 3.0 | 5.5 ± 3.7 | 1.9 ± 0.03 |
| TRN | -0.08 ± 0.09 | -0.009 ± 0.007 | 0.041 ± 0.026 | 415.9 ± 13.7 | 415.7 ± 21.0 | 12.2 ± 10.7 | 2.8 ± 5.4 | 3.1 ± 6.1 | 1.9 ± 0.04 |
| BIR | -0.09 ± 0.1 | - | - | 410.7 ± 7.6 | 410.6 ± 10.3 | 6.1 ± 4.1 | - | - | - |
| CMN | -0.03 ± 0.05 | - | - | 408.4 ± 6.7 | 408.2 ± 8.8 | 5.1 ± 2.6 | - | - | - |
| HEL | -0.15 ± 0.25 | - | - | 414.1 ± 9.3 | 414.2 ± 16.7 | 11.1 ± 6.9 | - | - | - |
| IPR | -0.04 ± 0.05 | - | - | 428.8 ± 17.6 | 428.8 ± 26.0 | 16.8 ± 10.3 | - | - | - |
| JUE | -0.07 ± 0.08 | - | - | 417.6 ± 15.3 | 416.9 ± 24.8 | 15.2 ± 15.5 | - | - | - |
| LMP | -0.01 ± 0.27 | - | - | 410.5 ± 4.6 | 410.3 ± 6.5 | 4.5 ± 1.8 | - | - | - |
| LUT | -0.1 ± 0.14 | - | - | 416.8 ± 15.7 | 416.8 ± 24.9 | 14.4 ± 12.7 | - | - | - |
| PRS | -0.02 ± 0.04 | - | - | 408.9 ± 5.0 | 409.0 ± 6.7 | 4.0 ± 2.0 | - | - | - |
| PUI | -0.07 ± 0.12 | - | - | 410.9 ± 6.1 | 411.0 ± 8.1 | 5.1 ± 2.2 | - | - | - |
| PUY | -0.06 ± 0.08 | - | - | 409.4 ± 8.3 | 409.3 ± 11.5 | 6.5 ± 4.2 | - | - | - |
| RGL | -0.11 ± 0.13 | - | - | 409.6 ± 8.3 | 409.6 ± 11.1 | 6.9 ± 3.9 | - | - | - |
| SMR | -0.07 ± 0.13 | - | - | 414.2 ± 10.6 | 414.2 ± 13.9 | 7.9 ± 4.6 | - | - | - |
| SSL | -0.06 ± 0.06 | - | - | 410.2 ± 6.6 | 410.4 ± 9.7 | 6.4 ± 3.1 | - | - | - |
| TOH | -0.06 ± 0.09 | - | - | 414.7 ± 11.7 | 414.9 ± 16.4 | 9.8 ± 5.6 | - | - | - |
| UTO | -0.24 ± 0.45 | - | - | 414.2 ± 9.2 | 414.3 ± 14.5 | 9.4 ± 5.0 | - | - | - |
| WAO | -0.06 ± 0.07 | - | - | 419.5 ± 9.6 | 420.2 ± 19.5 | 14.0 ± 7.5 | - | - | - |
| WES | -0.08 ± 0.12 | - | - | 414.1 ± 10.3 | 414.2 ± 18.6 | 13.0 ± 6.9 | - | - | - |
| ZSF | -0.03 ± 0.04 | - | - | 409.1 ± 5.3 | 409.2 ± 7.4 | 4.7 ± 2.3 | - | - | - |

## Appendix B: Spatial clustering algorithm

The inversion solves for offsets to the prior fluxes at a variable spatial resolution: high (up to 0.25°) in the direct vicinity of observation sites, but lower in parts of the domain that are not well sampled by the observation network. To achieve this, the spatial domain of the inversion is divided into a set of clusters of grid cells, each defined by the following properties:

- cells: the list of grid cells included in the cluster.
- weight: the sum of a property carried by each grid cell. In our case, this property is the average sensitivity of the observation network to that grid cell.
- size: the number of grid cells in the cluster.
- mean_lat, mean_lon: the average (area-weighted) lat and lon of the grid cells in the cluster
- area: the total of all the grid cells included in the cluster.
- type: ocean, land, or mixed.
- continuity: whether it is possible to "walk" from any grid cell of the cluster to any other one or whether there are discontinuities (e.g. a "land" cluster separated in two parts by ocean grid cells).

The objective of the clustering algorithm is to divide the domain into a user-defined number of continuous clusters with roughly equal "weight". The "weight" of a single grid cell is, in our case, defined as the average value of the adjoint field in that grid cell for an adjoint simulation driven by model-data mismatches set proportional to the uncertainty of each observation. The clustering is performed iteratively as follows:

1. Initially, one single cluster is formed, comprising all grid cells of the domain. It is added to a pool of "dividable" clusters.
2. The "weight" of all clusters in that pool is calculated (i.e. the weight of the single initial cluster at the first iteration);
3. The cluster with the largest weight is then split into two even parts across its longest axis (i.e., in an eastern and western part, at the first iteration);
4. The resulting two new clusters are checked for continuity. If needed, they are further split into several continuous clusters;
5. If a cluster reaches the minimum size (1 grid cell), it is moved to a pool of "defined" clusters.
6. If the total number of clusters ("dividable" plus "defined") is lower than the target number of clusters, then repeat steps 2 to 6. Otherwise, exit.

Because of how the cluster weights are defined, clusters away from observation points end up being considerably larger, but they are in regions where the inversions would have applied very smooth flux adjustments, so there is no real drawback to this clustering.

*Author contributions.* All authors designed the experiments, CG and GM developed the code, SB provided the $\Delta^{14}CO_2$ data, and CG performed the simulations. CG prepared the paper, and GM, SB, and MS provided corrections and suggestions for improvements.

*Competing interests.* The authors declare that they have no conflict of interest.

*Acknowledgements.* We thank the Swedish Research Council for Sustainable Development FORMAS for funding the 14C-FFDAS project (Dnr 2018-01771). MS, GM, and CG acknowledge support from the EU projects AVENGERS (Grant Agreement (GA): 101081322) and CORSO (GA: 101082194) as well as from the three Swedish strategic research areas ModElling the Regional and Global ~~earth~~ Earth system (MERGE), the e-science collaboration (eSSENCE), and Biodiversity and Ecosystems in a Changing Climate (BECC). SB acknowledges the National Aeronautics and Space Administration NASA grant 80NSSC21K1708 and NASA/ESSIC cooperative agreement 80NSSC23M0011. The computations were enabled by resources provided by the National Academic Infrastructure for Supercomputing in Sweden (NAISS), the Swedish National Infrastructure for Computing (SNIC) at LUNARC, and NSC partially funded by the Swedish Research Council through grant agreements no. 2022-06725 and no. 2018-05973, and the Royal Physiographic Society of Lund through Endowments for the Natural Sciences, Medicine and Technology - Geoscience.

## References

Aleksankina, K., Heal, M. R., Dore, A. J., Van Oijen, M., and Reis, S.: Global sensitivity and uncertainty analysis of an atmospheric chemistry transport model: The FRAME model (version 9.15.0) as a case study, Geoscientific Model Development, 11, 1653–1664, https://doi.org/10.5194/GMD-11-1653-2018, 2018.

Andres, R. J., Gregg, J. S., Losey, L., Marland, G., and Boden, T. A.: Monthly, global emissions of carbon dioxide from fossil fuel consumption, Tellus, Series B: Chemical and Physical Meteorology, 63, 309–327, https://doi.org/10.1111/J.1600-0889.2011.00530.X, 2011.

Andres, R. J., Boden, T. A., and Higdon, D. M.: Gridded uncertainty in fossil fuel carbon dioxide emission maps, a CDIAC }example, Atmospheric Chemistry and Physics, 16, 14 979–14 995, https://doi.org/10.5194/acp-16-14979-2016, 2016.

Basu, S., Guerlet, S., Butz, A., Houweling, S., Hasekamp, O., Aben, I., Krummel, P., Steele, P., Langenfelds, R., Torn, M., Biraud, S., Stephens, B., Andrews, A., and Worthy, D.: Global CO2 fluxes estimated from GOSAT retrievals of total column CO2, Atmos. Chem. Phys., 13, 8695–8717, https://doi.org/10.5194/acp-13-8695-2013, 2013.

Basu, S., Miller, J. B., and Lehman, S.: Separation of biospheric and fossil fuel fluxes of CO2 by }atmospheric inversion of CO2 and 14CO2 measurements: Observation System Simulations, Atmos. Chem. Phys., 16, 5665–5683, https://doi.org/10.5194/acp-16-5665-2016, 2016.

Basu, S., Lehman, S. J., Miller, J. B., Andrews, A. E., Sweeney, C., Gurney, K. R., Xu, X., Southon, J., and Tans, P. P.: Estimating US fossil fuel CO2 emissions from measurements of 14C in atmospheric CO2, Proceedings of the National Academy of Sciences, 117, 13 300–13 307, https://doi.org/10.1073/pnas.1919032117, 2020.

Bocquet, M., Elbern, H., Eskes, H., Hirtl, M., Žabkar, R., Carmichael, G. R., Flemming, J., Inness, A., Pagowski, M., Pérez Camaño, J. L., Saide, P. E., San Jose, R., Sofiev, M., Vira, J., Baklanov, A., Carnevale, C., Grell, G., and Seigneur, C.: Data assimilation in atmospheric chemistry models: current status and future prospects for coupled chemistry meteorology models, Atmos. Chem. Phys., 15, 5325–5358, https://doi.org/10.5194/acp-15-5325-2015, 2015.

Bréon, F. M., Broquet, G., Puygrenier, V., Chevallier, F., Xueref-Remy, I., Ramonet, M., Dieudonné, E., Lopez, M., Schmidt, M., Perrussel, O., and Ciais, P.: An attempt at estimating Paris area CO2 emissions from atmospheric concentration measurements, Atmos. Chem. Phys., 15, 1707–1724, https://doi.org/10.5194/acp-15-1707-2015, 2015.

Brioude, J., Angevine, W. M., Ahmadov, R., Kim, S.-W., Evan, S., McKeen, S. A., Hsie, E.-Y., Frost, G. J., Neuman, J. A., Pollack, I. B., Peischl, J., Ryerson, T. B., Holloway, J., Brown, S. S., Nowak, J. B., Roberts, J. M., Wofsy, S. C., Santoni, G. W., Oda, T., and Trainer, M.: Top-down estimate of surface flux in the Los Angeles Basin using a mesoscale inverse modeling technique: assessing anthropogenic emissions of CO, NO<sub>x</sub> and CO<sub>2</sub> and their impacts, Atmos. Chem. Phys., 13, 3661–3677, https://doi.org/10.5194/acp-13-3661-2013, 2013.

Chatterjee, A. and Michalak, A. M.: Technical Note: Comparison of ensemble Kalman filter and variational approaches for CO<sub>2</sub> data assimilation, Atmos. Chem. Phys., 13, 11 643–11 660, https://doi.org/10.5194/acp-13-11643-2013, 2013.

Chevallier, F., Bréon, F.-M., and Rayner, P. J.: Contribution of the Orbiting Carbon Observatory to the estimation of CO2 sources and sinks: Theoretical study in a variational data assimilation framework, Journal of Geophysical Research: Atmospheres, 112, https://doi.org/https://doi.org/10.1029/2006JD007375, 2007.

Eyring, V., Gillett, N. P., Achuta Rao, K. M., Barimalala, R., Barreiro Parrillo, M., Bellouin, N., Cassou, C., Durack, P. J., Kosaka, Y., McGregor, S., Min, S., Morgenstern, O., and Sun, Y.: Human Influence on the Climate System, in: Climate Change 2021: The Physical Science Basis. Contribution of Working Group I to the Sixth Assessment Report of the Intergovernmental Panel on Climate Change, edited by Masson-Delmotte, V., Zhai, P., Pirani, A., Connors, S. L., Péan, C., Berger, S., Caud, N., Chen, Y., Goldfarb, L., Gomis, M. I., Huang, M., Leitzell, K., Lonnoy, E., Matthews, J. B. R., Maycock, T. K., Waterfield, T., Yelekçi, O., Yu, R., and Zhou, B., p. 423–552, Cambridge University Press, Cambridge, United Kingdom and New York, NY, USA, https://doi.org/10.1017/9781009157896.005, 2021.

Gerbig, C. and Koch, F.-T.: Biosphere-atmosphere exchange fluxes for CO2 from the Vegetation Photosynthesis and Respiration Model VPRM for 2006-2022, https://doi.org/10.18160/VX78-HVA1, 2021a.

Gerbig, C. and Koch, F.-T.: European anthropogenic CO2 emissions based on EDGARv4.3, BP statistics 2021 and CarbonMonitor for 2019-2020 (Version 1.0). ICOS ERIC – Carbon Portal, https://doi.org/https://doi.org/10.18160/GFNT-5Y47, 2021b.

Graven, H., Fischer, M. L., Lueker, T., Jeong, S., Guilderson, T. P., Keeling, R. F., Bambha, R., Brophy, K., Callahan, W., Cui, X., Frankenberg, C., Gurney, K. R., Lafranchi, B. W., Lehman, S. J., Michelsen, H., Miller, J. B., Newman, S., Paplawsky, W., Parazoo, N. C., Sloop, C., and Walker, S. J.: Assessing fossil fuel CO2 emissions in California using atmospheric observations and models, Environmental Research Letters, 13, 065 007, https://doi.org/10.1088/1748-9326/AABD43, 2018.

Graven, H., Keeling, R. F., and Rogelj, J.: Changes to Carbon Isotopes in Atmospheric CO2 Over the Industrial Era and Into the Future, Global Biogeochemical Cycles, 34, e2019GB006 170, https://doi.org/https://doi.org/10.1029/2019GB006170, 2020.

Graven, H. D. and Gruber, N.: Continental-scale enrichment of atmospheric 14CO2 from the nuclear power industry: potential impact on the estimation of fossil fuel-derived CO2, Atmos. Chem. Phys., 11, 12 339–12 349, https://doi.org/10.5194/acp-11-12339-2011, 2011.

Hahn, V., Högberg, P., and Buchmann, N.: 14C – a tool for separation of autotrophic and heterotrophic soil respiration, Global Change Biology, 12, 972–982, https://doi.org/https://doi.org/10.1111/j.1365-2486.2006.001143.x, 2006.

Han, P., Zeng, N., Oda, T., Lin, X., Crippa, M., Guan, D., Janssens-Maenhout, G., Ma, X., Liu, Z., Shan, Y., Tao, S., Wang, H., Wang, R., Wu, L., Yun, X., Zhang, Q., Zhao, F., and Zheng, B.: Evaluating China's fossil-fuel CO2 emissions from a comprehensive dataset of nine inventories, Atmos. Chem. Phys., 20, 11 371–11 385, https://doi.org/10.5194/acp-20-11371-2020, 2020.

Hesshaimer, V. and Levin, I.: Revision of the stratospheric bomb 14CO2 inventory, Journal of Geophysical Research: Atmospheres, 105, 11 641–11 658, https://doi.org/https://doi.org/10.1029/1999JD901134, 2000.

Hesshaimer, V., Heimann, M., and Levin, I.: Radiocarbon evidence for a smaller oceanic carbon dioxide sink than previously believed, Nature, 370, 201–203, https://doi.org/10.1038/370201a0, 1994.

Hoffman, R. N. and Atlas, R.: Future Observing System Simulation Experiments, Bulletin of the American Meteorological Society, 97, 1601–1616, https://doi.org/10.1175/BAMS-D-15-00200.1, 2016.

ICOS, R. I., Apadula, F., Arnold, S., Bergamaschi, P., Biermann, T., Chen, H., Colomb, A., Conil, S., Couret, C., Cristofanelli, P., De Mazière, M., Delmotte, M., Emmenegger, L., Forster, G., Frumau, A., Hatakka, J., Heliasz, M., Heltai, D., Hensen, A., Hermansen, O., Hoheisel, A., Kneuer, T., Komínková, K., Kubistin, D., Laurent, O., Laurila, T., Lehner, I., Lehtinen, K., Leskinen, A., Leuenberger, M., Levula, J., Lindauer, M., Lopez, M., Lund Myhre, C., Lunder, C., Mammarella, I., Manca, G., Manning, A., Marek, M., Marklund, P., Meinhardt, F., Mölder, M., Müller-Williams, J., O'Doherty, S., Ottosson-Löfvenius, M., Piacentino, S., Pichon, J.-M., Pitt, J., Platt, S. M., Plaß-Dülmer, C., Ramonet, M., Rivas-Soriano, P., Roulet, Y.-A., Scheeren, B., Schmidt, M., Schumacher, M., Sha, M. K., Smith, P., Stanley, K., Steinbacher, M., Sørensen, L. L., Trisolino, P., Vítková, G., Yver-Kwok, C., and di Sarra, A.: ICOS Atmosphere Release 2023-1 of Level 2 Greenhouse Gas Mole Fractions of CO2, CH4, N2O, CO, meteorology and 14CO2, and flask samples analysed for CO2, CH4, N2O, CO, H2 and SF6, https://doi.org/10.18160/VXCS-95EV, 2023.

Janssens-Maenhout, G., Crippa, M., Guizzardi, D., Muntean, M., Schaaf, E., Dentener, F., Bergamaschi, P., Pagliari, V., Olivier, J. G. J., Peters, J. A. H. W., van Aardenne, J. A., Monni, S., Doering, U., Petrescu, A. M. R., Solazzo, E., and Oreggioni, G. D.: EDGAR v4.3.2 Global Atlas of the three major greenhouse gas emissions for the period 1970–2012, Earth Syst. Sci. Data, 11, 959–1002, https://doi.org/10.5194/essd-11-959-2019, 2019.

Kaminski, T., Scholze, M., Rayner, P., Voßbeck, M., Buchwitz, M., Reuter, M., Knorr, W., Chen, H., Agustí-Panareda, A., Löscher, A., and Meijer, Y.: Assimilation of atmospheric CO2 observations from space can support national CO2 emission inventories, Environmental Research Letters, 17, 014 015, https://doi.org/10.1088/1748-9326/ac3cea, 2022.

Kuc, T., Rozanski, K., Zimnoch, M., Necki, J. M., and Korus, A.: Anthropogenic emissions of CO2 and CH4 in an urban environment, Applied Energy, 75, 193–203, https://doi.org/https://doi.org/10.1016/S0306-2619(03)00032-1, 2003.

Kuhlmann, G., Henne, S., Meijer, Y., and Brunner, D.: Quantifying CO2 Emissions of Power Plants With CO2 and NO2 Imaging Satellites, Frontiers in Remote Sensing, 2, https://www.frontiersin.org/articles/10.3389/frsen.2021.689838, 2021.

Lehman, S. J., Miller, J. B., Wolak, C., Southon, J., Tans, P. P., Montzka, S. A., Sweeney, C., Andrews, A., LaFranchi, B., Guilderson, T. P., and Turnbull, J. C.: Allocation of Terrestrial Carbon Sources Using 14CO2: Methods, Measurement, and Modeling, Radiocarbon, 55, 1484–1495, https://doi.org/DOI: 10.1017/S0033822200048414, 2013.

Lehmuskoski, J., Vasama, H., Hämäläinen, J., Hokkinen, J., Kärkelä, T., Heiskanen, K., Reinikainen, M., Rautio, S., Hirvelä, M., and Genoud, G.: On-Line Monitoring of Radiocarbon Emissions in a Nuclear Facility with Cavity Ring-Down Spectroscopy, Analytical Chemistry, 93, 16 096–16 104, https://doi.org/10.1021/acs.analchem.1c03814, 2021.

Levin, I. and Hesshaimer, V.: Radiocarbon – A Unique Tracer of Global Carbon Cycle Dynamics, Radiocarbon, 42, 69–80, https://doi.org/DOI: 10.1017/S0033822200053066, 2000.

Levin, I. and Karstens, U.: Inferring high-resolution fossil fuel CO2 records at continental sites from combined 14CO2 and CO observations, Tellus B, 59, 245–250, https://doi.org/https://doi.org/10.1111/j.1600-0889.2006.00244.x, 2007.

Levin, I., Hammer, S., Kromer, B., and Meinhardt, F.: Radiocarbon observations in atmospheric CO2: Determining fossil fuel CO2 over Europe using Jungfraujoch observations as background, Science of The Total Environment, 391, 211–216, https://doi.org/https://doi.org/10.1016/j.scitotenv.2007.10.019, 2008.

Levin, I., Karstens, U., Eritt, M., Maier, F., Arnold, S., Rzesanke, D., Hammer, S., Ramonet, M., Vítková, G., Conil, S., Heliasz, M., Kubistin, D., and Lindauer, M.: A dedicated flask sampling strategy developed for Integrated Carbon Observation System (ICOS) stations based on CO2 and CO measurements and Stochastic Time-Inverted Lagrangian Transport (STILT) footprint modelling, Atmos. Chem. Phys., 20, 11 161–11 180, https://doi.org/10.5194/acp-20-11161-2020, 2020.

Locatelli, R., Bousquet, P., Hourdin, F., Saunois, M., Cozic, A., Couvreux, F., Grandpeix, J. Y., Lefebvre, M. P., Rio, C., Bergamaschi, P., Chambers, S. D., Karstens, U., Kazan, V., Van Der Laan, S., Meijer, H. A., Moncrieff, J., Ramonet, M., Scheeren, H. A., Schlosser, C., Schmidt, M., Vermeulen, A., and Williams, A. G.: Atmospheric transport and chemistry of trace gases in LMDz5B: Evaluation and implications for inverse modelling, Geoscientific Model Development, 8, 129–150, https://doi.org/10.5194/GMD-8-129-2015, 2015.

Mahadevan, P., Wofsy, S. C., Matross, D. M., Xiao, X., Dunn, A. L., Lin, J. C., Gerbig, C., Munger, J. W., Chow, V. Y., and Gottlieb, E. W.: A satellite-based biosphere parameterization for net ecosystem CO2 exchange: Vegetation Photosynthesis and Respiration Model (VPRM), Global Biogeochemical Cycles, 22, https://doi.org/https://doi.org/10.1029/2006GB002735, 2008.

Miller, J. B., Lehman, S. J., Montzka, S. A., Sweeney, C., Miller, B. R., Karion, A., Wolak, C., Dlugokencky, E. J., Southon, J., Turnbull, J. C., and Tans, P. P.: Linking emissions of fossil fuel CO2 and other anthropogenic trace gases using atmospheric 14CO2, Journal of Geophysical Research: Atmospheres, 117, https://doi.org/https://doi.org/10.1029/2011JD017048, 2012.

Monteil, G. and Scholze, M.: Regional CO2 inversions with LUMIA, the Lund University Modular Inversion Algorithm, v1.0, Geosci. Model Dev., 14, 3383–3406, https://doi.org/10.5194/gmd-14-3383-2021, 2021.

Monteil, G., Broquet, G., Scholze, M., Lang, M., Karstens, U., Gerbig, C., Koch, F.-T., Smith, N. E., Thompson, R. L., Luijkx, I. T., White, E., Meesters, A., Ciais, P., Ganesan, A. L., Manning, A., Mischurow, M., Peters, W., Peylin, P., Tarniewicz, J., Rigby, M., Rödenbeck, C., Vermeulen, A., and Walton, E. M.: The regional European atmospheric transport inversion comparison, EUROCOM: first results on European-wide terrestrial carbon fluxes for the period 2006–2015, Atmos. Chem. Phys., 20, 12 063–12 091, https://doi.org/10.5194/acp-20-12063-2020, 2020.

Munassar, S., Monteil, G., Scholze, M., Karstens, U., Rödenbeck, C., Koch, F. T., Totsche, K. U., and Gerbig, C.: Why do inverse models disagree? A case study with two European CO2 inversions, Atmospheric Chemistry and Physics, 23, 2813–2828, https://doi.org/10.5194/ACP-23-2813-2023, 2023.

Naegler, T. and Levin, I.: Closing the global radiocarbon budget 1945–2005, Journal of Geophysical Research: Atmospheres, 111, https://doi.org/https://doi.org/10.1029/2005JD006758, 2006.

Newman, S., Jeong, S., Fischer, M. L., Xu, X., Haman, C. L., Lefer, B., Alvarez, S., Rappenglueck, B., Kort, E. A., Andrews, A. E., Peischl, J., Gurney, K. R., Miller, C. E., and Yung, Y. L.: Diurnal tracking of anthropogenic CO2 emissions in the Los Angeles basin megacity during spring 2010, Atmos. Chem. Phys., 13, 4359–4372, https://doi.org/10.5194/acp-13-4359-2013, 2013.

Oda, T. and Maksyutov, S.: A very high-resolution (1km×1 km) global fossil fuel CO2 emission inventory derived using a point source database and satellite observations of nighttime lights, Atmospheric Chemistry and Physics, 11, 543–556, https://doi.org/10.5194/ACP-11-543-2011, 2011.

Oda, T. and Maksyutov, S.: ODIAC Fossil Fuel CO2 Emissions Dataset (Version name: ODIAC2020b), https://doi.org/10.17595/20170411.001, 2020.

Oda, T., Maksyutov, S., and Andres, R. J.: The Open-source Data Inventory for Anthropogenic CO2, version 2016 (ODIAC2016): a global monthly fossil fuel CO2 gridded emissions data product for tracer transport simulations and surface flux inversions, Earth Syst. Sci. Data, 10, 87–107, https://doi.org/10.5194/essd-10-87-2018, 2018.

Pickers, P. A., Manning, A. C., Le Quéré, C., Forster, G. L., Luijkx, I. T., Gerbig, C., Fleming, L. S., and Sturges, W. T.: Novel quantification of regional fossil fuel CO2 reductions during COVID-19 lockdowns using atmospheric oxygen measurements, Science Advances, 8, eabl9250, https://doi.org/10.1126/sciadv.abl9250, 2022.

Pisso, I., Sollum, E., Grythe, H., Kristiansen, N. I., Cassiani, M., Eckhardt, S., Arnold, D., Morton, D., Thompson, R. L., Groot Zwaaftink, C. D., Evangeliou, N., Sodemann, H., Haimberger, L., Henne, S., Brunner, D., Burkhart, J. F., Fouilloux, A., Brioude, J., Philipp, A., Seibert, P., and Stohl, A.: The Lagrangian particle dispersion model FLEXPART version 10.4, Geosci. Model Dev., 12, 4955–4997, https://doi.org/10.5194/gmd-12-4955-2019, 2019.

Rayner, P. J., Michalak, A. M., and Chevallier, F.: Fundamentals of data assimilation applied to biogeochemistry, Atmos. Chem. Phys., 19, 13 911–13 932, https://doi.org/10.5194/acp-19-13911-2019, 2019.

Rödenbeck, C., Gerbig, C., Trusilova, K., and Heimann, M.: A two-step scheme for high-resolution regional atmospheric trace gas inversions based on independent models, Atmos. Chem. Phys., 9, 5331–5342, https://doi.org/10.5194/acp-9-5331-2009, 2009.

Rödenbeck, C., Keeling, R. F., Bakker, D. C. E., Metzl, N., Olsen, A., Sabine, C., and Heimann, M.: Global surface-ocean pCO2 and sea–air CO2 flux variability from an observation-driven ocean mixed-layer scheme, Ocean Sci., 9, 193–216, https://doi.org/10.5194/os-9-193-2013, 2013.

Scholze, M., Kaplan, J. O., Knorr, W., and Heimann, M.: Climate and interannual variability of the atmosphere-biosphere 13CO2 flux, Geophysical Research Letters, 30, https://doi.org/https://doi.org/10.1029/2002GL015631, 2003.

Scholze, M., Buchwitz, M., Dorigo, W., Guanter, L., and Quegan, S.: Reviews and syntheses: Systematic Earth observations for use in terrestrial carbon cycle data assimilation systems, Biogeosciences, 14, 3401–3429, https://doi.org/10.5194/bg-14-3401-2017, 2017.

Schuh, A. E., Jacobson, A. R., Basu, S., Weir, B., Baker, D., Bowman, K., Chevallier, F., Crowell, S., Davis, K. J., Deng, F., Denning, S., Feng, L., Jones, D., Liu, J., and Palmer, P. I.: Quantifying the Impact of Atmospheric Transport Uncertainty on CO2 Surface Flux Estimates, Global Biogeochemical Cycles, 33, 484–500, https://doi.org/10.1029/2018GB006086, 2019.

Shiga, Y. P., Michalak, A. M., Gourdji, S. M., Mueller, K. L., and Yadav, V.: Detecting fossil fuel emissions patterns from subcontinental regions using North American in situ CO2 measurements, Geophysical Research Letters, 41, 4381–4388, https://doi.org/https://doi.org/10.1002/2014GL059684, 2014.

Smith, B., Wårlind, D., Arneth, A., Hickler, T., Leadley, P., Siltberg, J., and Zaehle, S.: Implications of incorporating N cycling and N limitations on primary production in an individual-based dynamic vegetation model, Biogeosciences, 11, 2027–2054, https://doi.org/10.5194/bg-11-2027-2014, 2014.

Solazzo, E., Crippa, M., Guizzardi, D., Muntean, M., Choulga, M., and Janssens-Maenhout, G.: Uncertainties in the Emissions Database for Global Atmospheric Research (EDGAR) emission inventory of greenhouse gases, Atmos. Chem. Phys., 21, 5655–5683, https://doi.org/10.5194/acp-21-5655-2021, 2021.

Steinbach, J., Gerbig, C., Rödenbeck, C., Karstens, U., Minejima, C., and Mukai, H.: The CO<sub>2</sub> release and Oxygen uptake from Fossil Fuel Emission Estimate (COFFEE) dataset: effects from varying oxidative ratios, Atmos. Chem. Phys., 11, 6855–6870, https://doi.org/10.5194/acp-11-6855-2011, 2011.

Stuiver, M. and Polach, H. A.: Discussion Reporting of 14C Data, Radiocarbon, 19, 355–363, https://doi.org/DOI: 10.1017/S0033822200003672, 1977.

Suess, H. E.: Radiocarbon Concentration in Modern Wood, Science, 122, 415–417, https://doi.org/10.1126/science.122.3166.415.b, 1955.

Tans, P. P., De Jong, A. F. M., and Mook, W. G.: Natural atmospheric 14C variation and the Suess effect, Nature, 280, 826–828, https://doi.org/10.1038/280826a0, 1979.

Thompson, R. L., Broquet, G., Gerbig, C., Koch, T., Lang, M., Monteil, G., Munassar, S., Nickless, A., Scholze, M., Ramonet, M., Karstens, U., van Schaik, E., Wu, Z., and Rödenbeck, C.: Changes in net ecosystem exchange over Europe during the 2018 drought based on atmospheric observations, Philosophical Transactions of the Royal Society B: Biological Sciences, 375, 20190 512, https://doi.org/10.1098/rstb.2019.0512, 2020.

Trumbore, S. E., Sierra, C. A., and Hicks Pries, C. E.: Radiocarbon Nomenclature, Theory, Models, and Interpretation: Measuring Age, Determining Cycling Rates, and Tracing Source Pools, in: Radiocarbon and Climate Change: Mechanisms, Applications and Laboratory Techniques, edited by Schuur, E. A. G., Druffel, E., and Trumbore, S. E., pp. 45–82, Springer International Publishing, Cham, https://doi.org/10.1007/978-3-319-25643-6_3, 2016.

Turnbull, J., Rayner, P., Miller, J., Naegler, T., Ciais, P., and Cozic, A.: On the use of 14CO2 as a tracer for fossil fuel CO2: Quantifying uncertainties using an atmospheric transport model, Journal of Geophysical Research: Atmospheres, 114, https://doi.org/https://doi.org/10.1029/2009JD012308, 2009.

Turnbull, J. C., Keller, E. D., Baisden, T., Brailsford, G., Bromley, T., Norris, M., and Zondervan, A.: Atmospheric measurement of point source fossil CO2 emissions, Atmos. Chem. Phys., 14, 5001–5014, https://doi.org/10.5194/acp-14-5001-2014, 2014.

Turnbull, J. C., Sweeney, C., Karion, A., Newberger, T., Lehman, S. J., Tans, P. P., Davis, K. J., Lauvaux, T., Miles, N. L., Richardson, S. J., Cambaliza, M. O., Shepson, P. B., Gurney, K., Patarasuk, R., and Razlivanov, I.: Toward quantification and source sector identification of fossil fuel CO2 emissions from an urban area: Results from the INFLUX experiment, Journal of Geophysical Research: Atmospheres, 120, 292–312, https://doi.org/10.1002/2014JD022555, 2015.

Turnbull, J. C., Graven, H., and Krakauer, N. Y.: Radiocarbon in the Atmosphere, in: Radiocarbon and Climate Change: Mechanisms, Applications and Laboratory Techniques, edited by Schuur, E. A. G., Druffel, E., and Trumbore, S. E., pp. 83–137, Springer International Publishing, Cham, https://doi.org/10.1007/978-3-319-25643-6_4, 2016.

Turnbull, J. C., Domingues, L. G., and Turton, N.: Dramatic Lockdown Fossil Fuel CO2 Decrease Detected by Citizen Science-Supported Atmospheric Radiocarbon Observations, Environmental Science & Technology, 56, 9882–9890, https://doi.org/10.1021/acs.est.1c07994, 2022.

UNFCCC: THE PARIS AGREEMENT, Tech. rep., https://treaties.un.org/Pages/ViewDetails.aspx?src=TREATY&mtdsg_no=XXVII-7-, 2016.

Vardag, S. N., Gerbig, C., Janssens-Maenhout, G., and Levin, I.: Estimation of continuous anthropogenic CO2: model-based evaluation of CO2, CO, $\delta$13C(CO2) and $\Delta$14C(CO2) tracer methods, Atmos. Chem. Phys., 15, 12 705–12 729, https://doi.org/10.5194/acp-15-12705-2015, 2015.

Vogel, F. R., Levin, I., and Worthy, D. E. J.: Implications for Deriving Regional Fossil Fuel CO2 Estimates from Atmospheric Observations in a Hot Spot of Nuclear Power Plant 14CO2 Emissions, Radiocarbon, 55, 1556–1572, https://doi.org/DOI: 10.1017/S0033822200048487, 2013.

Wang, Y., Broquet, G., Ciais, P., Chevallier, F., Vogel, F., Wu, L., Yin, Y., Wang, R., and Tao, S.: Potential of European 14CO2 observation network to estimate the fossil fuel CO2 emissions via atmospheric inversions, Atmos. Chem. Phys., 18, 4229–4250, https://doi.org/10.5194/acp-18-4229-2018, 2018.

Wang, Y., Broquet, G., Bréon, F.-M., Lespinas, F., Buchwitz, M., Reuter, M., Meijer, Y., Loescher, A., Janssens-Maenhout, G., Zheng, B., and Ciais, P.: PMIF v1.0: assessing the potential of satellite observations to constrain CO2 emissions from large cities and point sources over the globe using synthetic data, Geosci. Model Dev., 13, 5813–5831, https://doi.org/10.5194/gmd-13-5813-2020, 2020.

Wu, Z.: European hourly NEE, GPP and total respiration for 2010-2022 based on LPJ-GUESS (generated in 2023), https://doi.org/10.18160/p52c-1qjm, 2023.

Zazzeri, G., Acuña Yeomans, E., and Graven, H. D.: Global and Regional Emissions of Radiocarbon from Nuclear Power Plants from 1972 to 2016, Radiocarbon, 60, 1067–1081, https://doi.org/DOI: 10.1017/RDC.2018.42, 2018.

Zazzeri, G., Graven, H., Xu, X., Saboya, E., Blyth, L., Manning, A. J., Chawner, H., Wu, D., and Hammer, S.: Radiocarbon Measurements Reveal Underestimated Fossil CH4 and CO2 Emissions in London, Geophysical Research Letters, 50, e2023GL103 834, https://doi.org/https://doi.org/10.1029/2023GL103834, 2023.